Crustal deformation and seismic velocity perturbations in the Alto Tiberina fault zone (Northern Apennines, Italy)

Carlos Almagro Vidal[1], Lucia Zaccarelli[2], Francesco Pintori[3], and Enrico Serpelloni[1]

[1]Istituto Nazionale di Geofisica e Vulcanologia
[2]INGV
[3]Dipartimento di Fisica e Astronomia, Settore di Geofisica, Università di Bologna

March 15, 2024

Abstract

Crustal perturbations related to seismic activity can generally be observed with the occurrence of a large magnitude event. For less energetic seismic sequences though, the associated transient crustal variations are questionably measurable, and their observation gets easily obscured by relatively stronger perturbations such as the ones related to hydrological processes. In this study we reveal the significant role that terrestrial water-storage variations play in governing temporal crustal changes in the tectonically active Northern Apennines of Italy, and discuss the potential of accounting for its correction in order to monitor the relatively weaker transient perturbations caused by local seismic swarms. This area is characterized by an extensive level of low-energetic seismic activity, typically clustered in time and space, of which three main seismic swarms outstand during the 12-year period of study (2010-2021). Our analysis compares independent observations and processing methods of GNSS measurements and ambient seismic noise recordings. We adopt a multivariate statistical approach to discriminate between independent sources of ground deformation, and seismic noise cross-correlation analysis to monitor relative seismic-velocity variations. The result shows how the perturbation effects produced by variations in total water content are dominant in both time series of ground deformations and seismic-velocity variations. After correcting for the water-related variation effects, our monitoring results reveal perturbations in the crustal properties whose activation time and depth range correlate with the occurrences of the seismic swarms.

Crustal deformation and seismic velocity perturbations in the Alto Tiberina fault zone (Northern Apennines, Italy)

C. Almagro Vidal[1], L. Zaccarelli[1], F. Pintori[1], and E. Serpelloni[1]

[1]National Institute of Geophysics and Volcanology - INGV Bologna

Key Points:

- Crustal-perturbation monitoring
- Ambient seismic noise
- Hydrological and seismic perturbations

Abstract

Crustal perturbations related to seismic activity can generally be observed with the occurrence of a large magnitude event. For less energetic seismic sequences though, the associated transient crustal variations are questionably measurable, and their observation gets easily obscured by relatively stronger perturbations such as the ones related to hydrological processes. In this study we reveal the significant role that terrestrial water-storage variations play in governing temporal crustal changes in the tectonically active Northern Apennines of Italy, and discuss the potential of accounting for its correction in order to monitor the relatively weaker transient perturbations caused by local seismic swarms. This area is characterized by an extensive level of low-energetic seismic activity, typically clustered in time and space, of which three main seismic swarms outstand during the 12 year period of study (2010-2021). Our analysis compares independent observations and processing methods of GNSS measurements and ambient seismic noise recordings. We adopt a multivariate statistical approach to discriminate between independent sources of ground deformation, and seismic noise cross-correlation analysis to monitor relative seismic-velocity variations. The result shows how the perturbation effects produced by variations in total water content are dominant in both time series of ground deformations and seismic-velocity variations. After correcting for the water-related variation effects, our monitoring results reveal perturbations in the crustal properties whose activation time and depth range correlate with the occurrences of the seismic swarms.

Plain Language Summary

The observation of changes in the Earth's crust, either as surface ground deformation or perturbations in its elastic properties, is crucial in the study of the earthquake nucleation process. When the occurrence of seismic events involves small magnitudes, however, these observations become hardly visible and get easily masked by other relatively-larger crustal changes induced by surface phenomena such as the hydrological cycle. Geodetic-data processing achieves to estimate different ground deformation responses induced by independent phenomena, separating that due to seismic origin from the ones induced by the hydrological cycle. When monitoring the crustal properties with ambient seismic noise, the separation of the perturbation by their different sources becomes rather challenging. In the case of our study, a fast approach involves the estimation of the hydrological cycle, and use it as a proxy to correct for the hydrologically-induced perturbations. With this correction, we observe an agreement between the crustal elastic properties' changes with the occurrence of local seismic swarms both in time and depth.

1 Introduction

Seasonal variations are common in many geophysical monitoring datasets. Ground displacements, as recorded by Global Navigation Satellite System (GNSS) networks, respond to a variety of multiscale processes causing seasonal deformation signals (e.g., Dong et al., 2002), and the understanding of the mechanisms behind this periodic deformation has recently brought a vast amount of literature with it (White et al., 2022, and references therein). Seasonal changes in elastic properties of the Earth's crust, as obtained from the analysis of seismic noise cross-correlations, are also described in the most recent literature (e.g., Meier et al., 2010; Hillers et al., 2014; Poli et al., 2020; Andajani et al., 2020; Fokker et al., 2021). Moreover, seasonal changes in seismicity rates, as the response to seasonal stress changes at seismogenic depths, have been observed in several tectonic settings (Bettinelli et al., 2008; D'Agostino et al., 2018; Pintori et al., 2021). Accounting for these seasonal signals is mandatory in order to accurately estimate trends and their changes, and to detect transient signals associated with tectonic processes and the earthquake preparatory phase, particularly in slowly deforming regions, where tectonic transients may be much smaller in amplitude than non tectonic seasonal signals. GNSS time responses due to the latter are often associated with climatic and hydrological processes (e.g., Pan et al., 2019; Riddell et al., 2020; Pintori et al., 2022). Additionally, seasonal signals can bring important information on underlying processes, such as groundwater or surface-water changes, with important implications in either the monitoring of hydrological resources or measuring the mechanical properties of the Earth. Silverii et al. (2016) showed that hydrological-recharge and -discharge processes in karstic aquifers of the Southern and Central Apennines (Italy) can produce deformation signals of both seasonal and transient nature in GNSS position time series. The hydrologically-induced transient signals, which are recorded also by Serpelloni et al. (2018) in the Southern Alps, are important to recognize not only because they can be used as indirect indicators of groundwater content, but also because they can be misinterpreted as transient tectonic signals.

The use of ambient seismic noise cross-correlation analysis has gained popularity in seismology in the study and monitoring of the elastic properties of the Earth's subsurface. One effective method for monitoring changes with ambient seismic noise is the description of the perturbations in the medium in terms of relative seismic-velocity variations (Snieder et al., 2002; Grêt et al., 2006; Campillo, 2006). This method is mostly being employed in the detection of coseismic perturbations and post-seismic relaxation effects after strong seismic events (Brenguier et al., 2008; Zaccarelli et al., 2011; Minato et al., 2012), or in monitoring perturbations in volcanic areas (Brenguier et al., 2008; Anggono et al., 2012; Budi-Santoso & Lesage, 2016). Since the beginning of the application of this noise-based analysis, it has been clear how the water content in the Earth's crust plays an important role in determining the relative seismic-velocity variations (Sens-Schönfelder & Wegler, 2006; Tsai, 2011; Hillers et al., 2014b), and in recent years it has also been used to monitor hydrological perturbations (Voisin et al., 2017; Clements & Denolle, 2018; Yates et al., 2019; Liu et al., 2020; Illien et al., 2022).

In this work we discuss the results obtained from the analysis of GNSS position time-series, seismic-velocity perturbations and groundwater content in the Northern Apennines of Italy. We focus on the Alto Tiberina Fault (ATF) area (see Fig.1a), where multidisciplinary measurements are guaranteed by dense monitoring networks. Since 2010, a Near Fault Observatory has been created in order to monitor ground deformation and seismicity through a multidisciplinary infrastructure (with seismological, geodetic, and geochemical measurements, Chiaraluce et al., 2014; EPOS, n.d.). The study area is located in the high strain-rate belt that runs along the regional divide of the Italian Apennines (Anderlini et al., 2016; Serpelloni et al., 2022). The most important geological feature here is the Alto Tiberina fault, an active low-angle (dip angle of 15°) normal fault, NNW trending and about 60 km long (e.g., Chiaraluce et al., 2007). The ATF and its hanging-wall high-angle faults account for $\sim 2\,{}^{mm}/_{y}$ out of the $3\,{}^{mm}/_{y}$ regional extension rate across the Northern Apennines (Anderlini et al., 2016). Historical catalogues in the Umbria-Marche region document several earthquakes with macroseismic estimate of magnitudes greater than $M_w = 5.5$ being the largest one a $M_w = 6.4$ in 1781 (Rovida et al., 2020), yet no large earthquakes are unequivocally associated with the ATF. Geodetic measurements suggest that the ATF is aseismically creeping at depths greater than 5 km (Anderlini et al., 2016; Vadacca et al., 2016), where it is well delineated by microseismicity. More importantly, the same area experiences low-energetic seismic swarms confined in the shallower, hanging-wall faults (Gualandi et al., 2017) with possible involvement of the ATF (Vuan et al., 2020). During the 12 year period (2010-2021) of study, the ATF area has been interested by a sustained seismic activity whose occurrence may be grouped into three main swarms (after Valoroso et al., 2017):

1. the *Pietralunga* swarm from 10 April 2010 to 5 May 2010, with maximum $M_w = 3.6$;
2. the *Città di Castello* swarm from 20 April 2013 to 20 May 2013, with maximum $M_w = 3.6$;
3. the *Gubbio* swarm that started on 26 August 2013 and lasted until the end of 2014, with a maximum $M_w = 3.9$ on 22 December 2013.

Fig.1b shows the daily occurrence of the whole ATF seismicity from 2010 to 2015, while the map in Fig.1c depicts the epicentral location of events of the three aforementioned seismic swarms. Afterwards the local seismicity did not show additional clusters, which may be also masked by the 2016 Central Italy seismic sequence.

The goal of this study is to analyze the main source of crustal deformation and seismic-velocity variations in the area during the 12 year period of observations, trying to discriminate among the different possible sources of perturbations, from the water content variations to the tectonic activity occurred up to 2015.

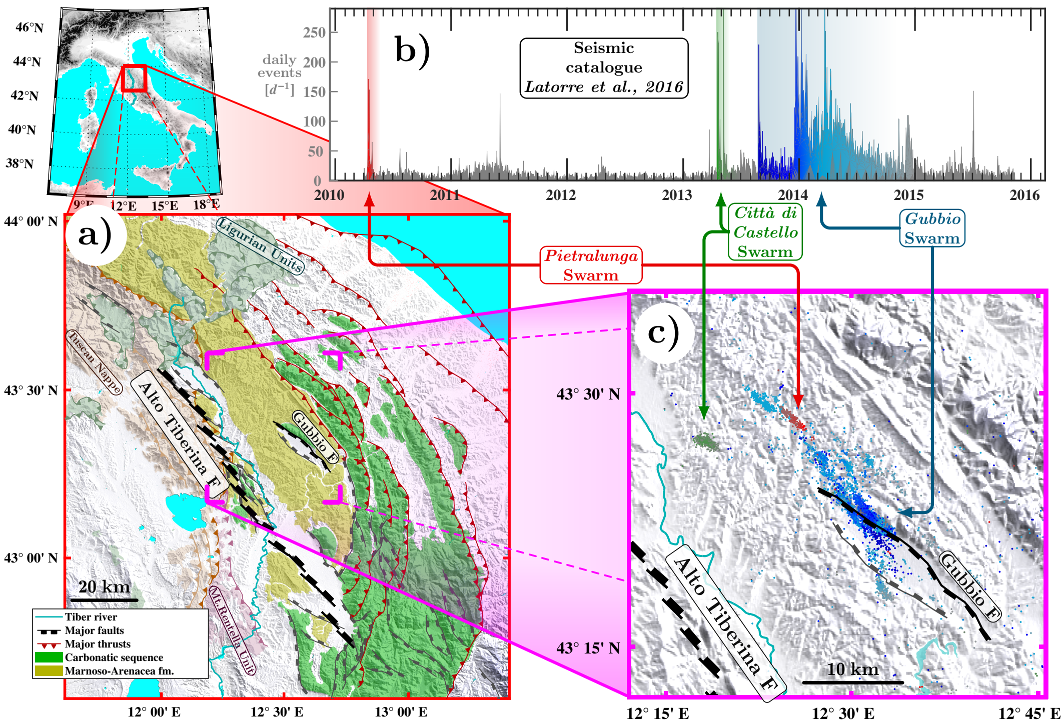

Figure 1: **a)** Location in the Italian peninsula and geological map of the ATF region, with the main tectonic units, formations, faults and thrusts. Inset showing the ATF region under study in the Italian peninsula. **b)** Temporal occurrence of the seismicity in the ATF area as the daily number of events along the 2010-2015 time period (Latorre et al., 2016): the red, green, and blue colors are used to distinguish between the *Pietralunga*, *Città di Castello* and *Gubbio* swarms, respectively. Color background highlights represent the start time and duration of each seismic swarm. **c)** Map of the epicentral locations of the local earthquake recorded during 2010-2015 (Latorre et al., 2016), in color agreement with panel b).

2 Data and Processing

In this section we describe the characteristics and processing of the different datasets included in this study: geodetic observations (GNSS), seismological recordings and meteoclimatic readings in the period between 1 January 2010 and Mid-February 2022. Every dataset acquisition network required a selection of GNSS/seismic/pluviometric stations within an area of ca. ~80 km radius set on the central section of the ATF-zone and comprising the upper Tiber basin (see Fig.2). In the case of the GNSS- and seismic- networks, the areas comprising the station selection are not limited to the upper Tiber basin, yet they sufficiently cover the watershed area.

2.1 GNSS

We use 33 GNSS stations, displayed in Fig.2a, and obtain the daily ground-displacement time series following the procedure described in Serpelloni et al. (2022). In order to increase the signal-to-noise ratio of the time series, we remove the common mode signal estimated at continental scale performing a Principal Component Analysis, as in Serpelloni et al. (2013). Furthermore, we remove the linear trend, which is estimated using the MIDAS software (Blewitt et al., 2016), from the GNSS time responses. Ultimately, we analyze the processed GNSS position time series using the Independent Component Analysis method with variational approximation and Bayesian inference (variational Bayesian ICA, Gualandi et al., 2016), which allows to separate statistically independent signals that are present in the time series. Assuming that the statistical independence of the signals means that they are caused by different processes, we associate each signal with a distinct geophysical process. In the case of this study we decompose the GNSS dataset in four Independent Components (IC's). This method has been successfully applied to extract hydrological and tectonic transient signals from geodetic displacement recordings (e.g., Gualandi et al., 2017; Serpelloni et al., 2018; Pintori et al., 2021); it uses a generative model to recreate the observations, allowing the extraction of the spatio-temporal information of an arbitrary number of independent sources of deformation from the observations, without imposing a priori any specific spatial distribution nor temporal function. The output is the definition of a limited number of sources, or IC's, characterized by a specific spatial coefficient distribution $U(\mathbf{x})$ (where $\mathbf{x}$ stands for the locations of the GNSS stations) and a time response $V(t)$. A weight coefficient is necessary to rescale their contribution in explaining the original displacement observation. In this study each IC is described by a mix of four Gaussian functions, allowing for more flexibility in the description of the sources with respect to classical ICA techniques and to consistently take into account data gaps in the displacement time series (K. Chan et al., 2003), providing also an estimate of the uncertainty associated with every IC. Hence, the displacement observations at a given station can be reconstructed by linearly summing up the contributions from all the IC's, each of which is obtained by multiplying together the specific spatial coefficient, the associated weight and the corresponding time response.

2.2 Seismic noise

We employ continuous seismic recordings from the Italian National Seismic Network (INGV Seismological Data Centre, 2006), and make a selection of 45 stations (short-period and broad-band), with a recording span longer than 6 years (see Fig.2b). For this analysis we concentrate on the seismic noise corresponding to oceanic microseisms (i.e., in the [0.1 1.0] Hz frequency range), and surface-wave signal reconstruction by cross-correlation. Our analysis involves vertical-component recordings only. Seismic processing includes standard instrumental correction, frequency band-pass filtering, spectral whitening and 1-bit normalization (Brenguier et al., 2008). Cross-correlations are carried out in 1 hour-long time sections, with half hour sliding (i.e., 50% of section overlap). In order to increase the signal reconstruction, a stacking of cross-correlation results is implemented in daily sequences. We test multiple stacking lengths to study the trade-off relation between quality in the seismic-signal reconstruction and lapse-time resolution (from 15 to 50 d). In this study we choose as most suitable the 30 d stacking-length result. We perform coda-wave interferometry (CWI, Snieder et al., 2002; Sens-Schönfelder & Wegler, 2006) on the first 26 s of seismic coda for every cross-correlation result. The analysis of the coda includes the estimate of 10 time-lag samples ($\delta\tau$) along the coda per surface-wave response. We apply a joint regression of the time lags $\delta\tau$ with respect to the coda-window time segment (τ) from all seismic-station pairs and calculate the coda-window relative time-lag variation $^{\delta\tau}/_{\tau}$. Assuming that the seismic perturbation is homogeneous throughout the study area, the final relative seismic-velocity variation ($^{\delta v}/_{v}$) is given by the linear relation $^{\delta v}/_{v} = {}^{-\delta\tau}/_{\tau}$ (Poupinet et al., 1984; Snieder, 2006).

We produce a first set of results from the cross-correlation analysis over the complete frequency range ([0.1 1.0] Hz). A second set of results is created with exactly the same processing but applied individually over six consecutive narrower frequency bands ([0.1 0.16], [0.16 0.25], [0.25 0.36], [0.36 0.5], [0.5 0.7] and [0.7 1.0] Hz). This second set of results allows us to investigate the scattering process at different frequency ranges and thus exploit the dispersive nature of the retrieved surface waves in order to explore the depth reach of the seismic perturbations in the crust. Although small in number, the choice and amount of frequency bands analyzed is a compromise between the partitioning of the frequency range of interest, the variation of the wavefield depth sensitivity extent and the stability of the cross-correlation signal in the time domain.

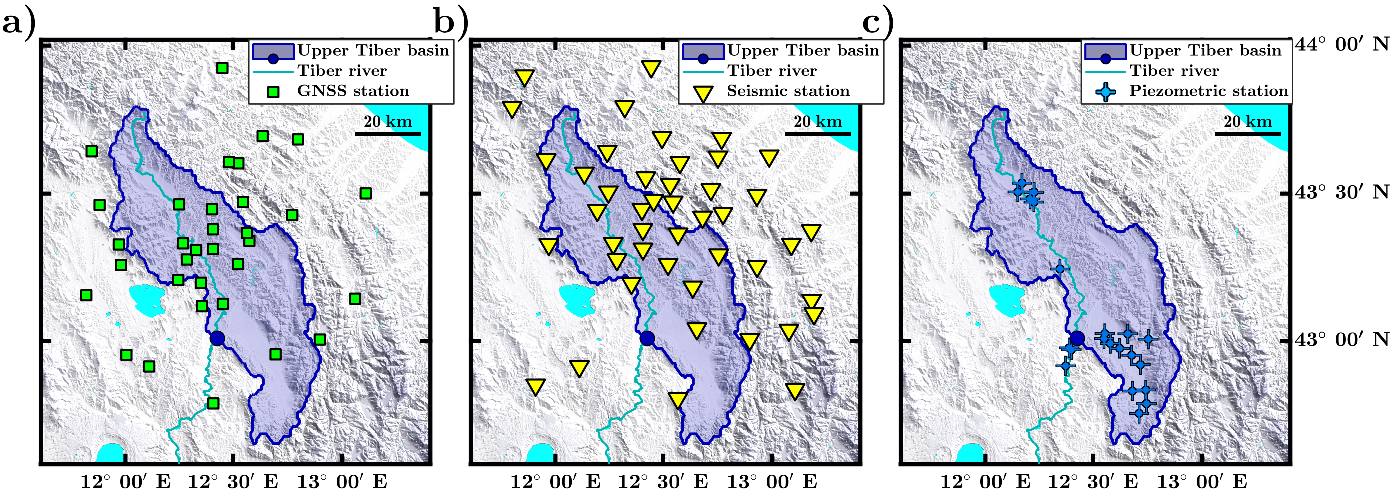

Figure 2: **a)** Location of the 33 continuous GNSS stations utilized. **b)** Distribution of the 45 permanent seismic stations of the Italian National Seismic Network selected for the seismic-noise analysis. **c)** Piezometric-sensor distribution (24) in the Umbria region used in this work. In all three panels the shadowed region depicts the upper Tiber basin taken into account for computing δTWS.

2.3 Meteo-climatic data

We take into account three kinds of meteo-climatic observations and processed data: the piezometric measurements, the hydrological balance in the upper Tiber basin in the form of total water storage variation, and the ground displacement associated with hydrological loading from a global gridded model. We calculate the Mean Piezometric Level (MPL) by performing an arithmetic mean of all the water-table readings available for this study in order to obtain an estimate representing the water-table variation in the whole upper Tiber basin. The piezometric level dataset is available at ARPA Umbria (2006) and the location of the 24 piezometric stations employed is shown in Fig.2c. In order for outlying values and single large-fluctuating piezometers not to dominate the ensemble average, we perform an amplitude normalization of every water-table reading beforehand prior to the arithmetic mean and add later an average of the respective mean values from every piezometer. We compute the total water storage variations (δTWS) in the upper Tiber basin following the method described in Pintori et al. (2021), by solving the mass balance equation between precipitation, evapotranspiration, incoming river inflow, outcoming river discharge, and potential groundwater import/export in a surrounding basin. Due to the difficulty in precisely estimating some of the parameters in the mass-balance equation, we exploit the GR5J rainfall-runoff model (Pushpalatha et al., 2011) for estimating the total water storage variations. The displacement time series associated with hydrological loading (hereinafter HL) is obtained considering the Land Surface Discharge Model (LSDM, developed by Dill, 2008). With this model approach, we estimate daily surface displacements from the continental hydrology by accounting for the precipitation, evaporation, and temperature from an atmospheric model developed by the European Centre for Medium Range Weather Forecasts (ECMWF, n.d.). We considered for this study the area with limits [11°30′E 13°E] in longitude and [43°N 44°N] in latitude.

From these three meteoclimatic products we thus obtain three independent observations related to the water content variations for the ATF zone. In Fig.4a, the δTWS and HL show a remarkable similarity and synchronized (but opposite) behaviour (-0.9 correlation coefficient). While HL is the result of a model that takes into account only the water stored in the first few meters of the subsurface, δTWS is influenced also by the groundwater. The strong similarity between HL and δTWS suggests that, in the upper Tiber basin, most of the water is stored as 'surface water' instead of groundwater, so that the groundwater-storage changes slightly influence the total water storage variations. On the other hand, the MPL time series in Fig.4b exhibits a different temporal behaviour, with more pronounced multi-annual variations (i.e., smaller maximum amplitudes for a drought period in 2012) and a persistent time delay with respect to both δTWS and HL (correlation coefficient of $\sim$0.7 and time lag of $\sim$30 d).

3 Results and Interpretation

3.1 GNSS IC decomposition

In Fig.3 we show the four IC's extracted from the GNSS-position time series. For each IC we show its corresponding time response ($V(t)$, right graph, normalized between -0.5 and 0.5) and spatial distribution ($U(\mathbf{x})$, left map). $V(t)$ describes how the displacement of the corresponding IC evolves with time, whereas $U(\mathbf{x})$ shows the maximum amplitude and 3D direction of the displacement at the location of every GNSS station $\mathbf{x}$. The color scale represents the amplitude of the maximum vertical displacement, while the yellow arrows indicate the maximum amplitude and orientation of the horizontal displacement. The displacement related to the ICn over a time interval $[t_1\ t_2]$ (with $t_2 > t_1$) at a station m is computed as $[V_n(t_2) - V_n(t_1)]\ U_n(\mathbf{x}_m)$, where $V_n(t)$ is the time response of the ICn and U_n is its corresponding spatial response.If $V_n(t)$ increases the station's horizontal displacement follows the yellow-arrow sense, while the vertical displacement is upward if the U_n vertical component is positive and downward if negative (see color scale in the maps of Fig.3).

IC1 in Fig.3 presents a clear sinusoidal behaviour with annual periodicity. The U_1 vertical components reveal a uniform response (except for one site on the NW margin). The vertical displacement of IC1's periodic signal holds a magnitude fluctuation of ca. $\sim$1 cm, while the horizontal displacement bears smaller amplitudes. Fig.4a shows the good agreement between IC1's time response and both δTWS and HL: the time series are strongly correlated (0.7 correlation coefficient) without significant time lag.

IC2 in Fig.3 shows a non-uniform spatial response both in the vertical and horizontal components. The time response of this IC exposes two different transients: the first in 2013-2014 and the second in 2016. The latter transient corresponds to the post-seismic deformation following the *Amatrice-Visso-Norcia* sequence in Central Italy, whose epicentral area is located 70-90 km south of the study area. The results are consistent, both in terms of temporal evolution and spatial response, with those presented in Mandler et al. (2021), and primarily affected the southernmost stations considered in our work. As regards the first transient signal, this is more complex to interpret. First, it shows some cross-talk with IC3. Secondly, it is of smaller entity with respect to both IC3 and the *Amatrice-Visso-Norcia* post-seismic signal. Tentatively, this small transient deformation could be associated with the *Città di Castello* seismic swarm, but the deformation pattern from the spatial response of GNSS stations in the ATF area is not that clear.

The IC3 time response also reveals a transient signal at the beginning of 2014, which is very similar both in terms of spatial distribution and temporal evolution to the one extracted by Gualandi et al. (2017). The coincidence of transient signals occurring at the end of 2013 in the time responses of both IC2 and IC3 makes it possible that cross-talk might have taken place between the two.

IC4 is described in Fig.3 as the weakest independent component in the analysis. Although its spatial coefficients show a non-uniform distribution, its time response exhibits a clear seasonal signal with a similar annual periodicity as IC1's. Fig.4b shows a good similarity of IC4's time response with the mean piezometric level at the upper Tiber basin, a solid correlation (0.7 correlation coefficient) and a ca. $\sim$30 d time lag. This suggests that the displacements associated with IC4 are related to variations of the deep portion of the water storage: we interpret the delay between the displacements and the piezometric-level variations as due to the time needed by the water to reach aquifers located deeper than the ones caught by the piezometers, whose median depth is shallower than 10 m. Furthermore, Silverii et al. (2016) and Pintori et al. (2021) interpreted a deformation pattern analogous to IC4's, characterized by anisotropic horizontal deformations with amplitudes similar to the vertical ones, caused by water-level variations in fracture systems beneath karst aquifers.

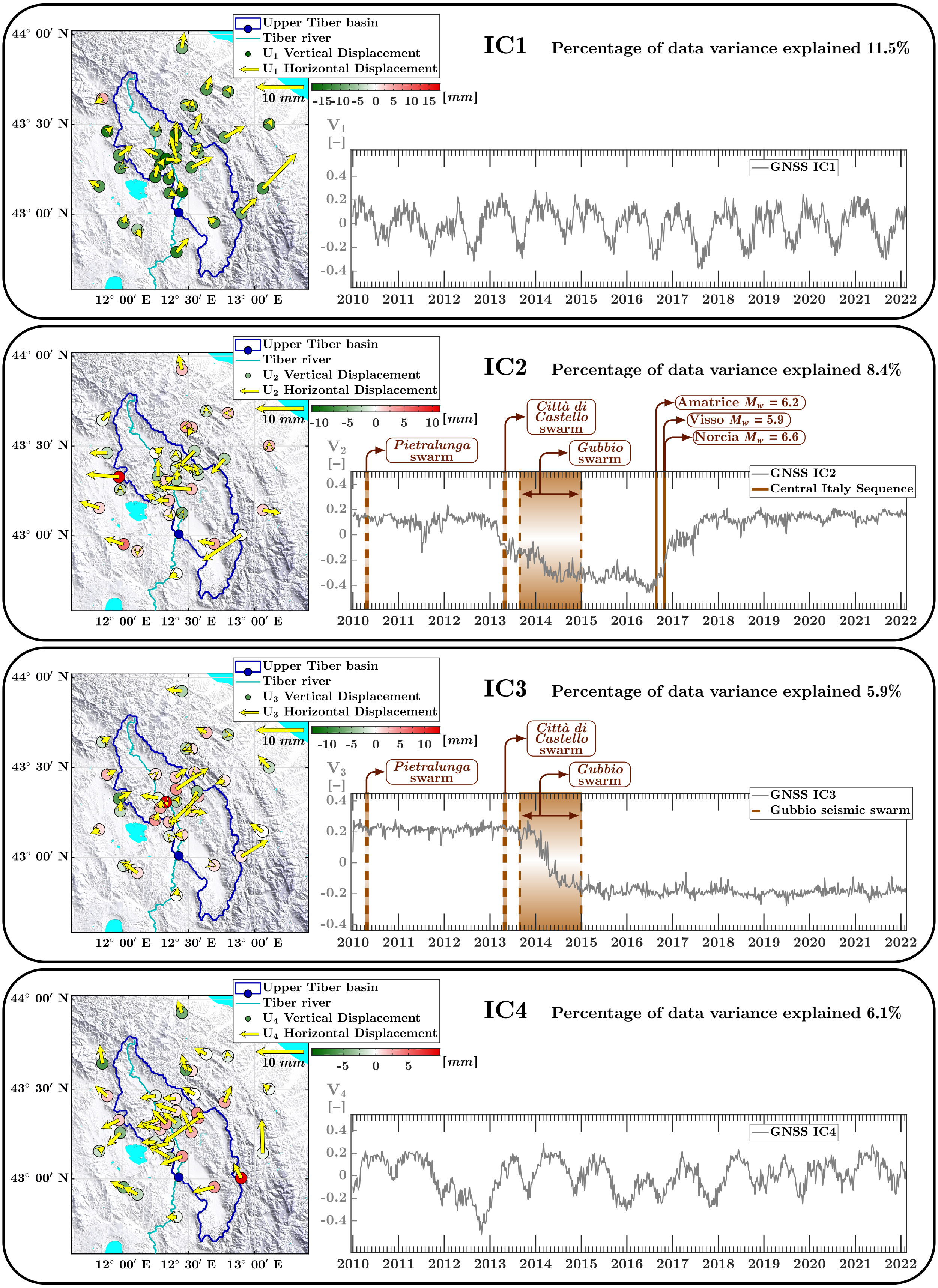

Figure 3: Time response $V_n(t)$ and spatial coefficients $U_n(\mathbf{x})$ of the four independent components: **IC1** , **IC2**, **IC3** and **IC4**. Labeled brown lines in IC2 and IC3 represent the occurrences of the three ATF seismic swarms (dashed and shadowed regions), and the three mainshocks of the Central Italy seismic sequence (solid).

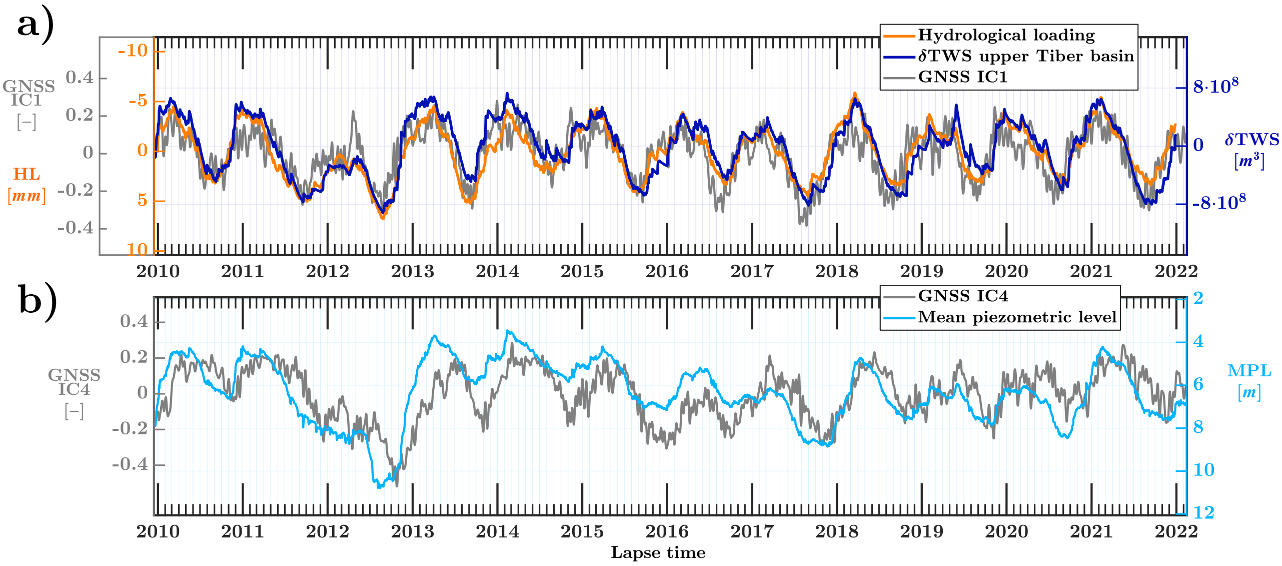

Figure 4: **a)** Time response of IC1 (namely $V_1(t)$ in Fig.3, gray) compared to the total water storage variation of the upper Tiber basin (δTWS, dark blue) and the vertical displacement caused by hydrological loading (HL, orange). Note that the HL's abscissa in the graph is reversed. **b)** Comparison between the mean piezometric level at the upper Tiber basin (MPL, light blue) and the IC4's time response (gray).

3.2 Seismic-velocity variations

In this section we present the results for the 12 year monitoring through ambient seismic noise cross-correlations. In Fig.5a we show the result of the daily-sampled relative seismic-velocity variations ($^{\delta v}/_{v}$, coloured-red line) obtained from the analysis of the data in the whole [0.1 1.0] Hz frequency band. Each daily $^{\delta v}/_{v}$ estimate is plotted at the end of the respective 30 d interval. The color scale stands for the number of $\delta\tau$ values considered in the $^{\delta\tau}/_{\tau}$ linear regression. This value represents a measure of the quality of the estimates and depends (among others) on the number of station pairs available. The color evolution, from yellow at the beginning of 2010, to red in 2012, shows how some of the employed stations have been installed during the first two years of analysis, meaning that the most stable and reliable measurements start from 2012.

For comparison, Fig.5a shows the total water storage variations of the upper Tiber basin and the IC1 temporal evolution (Fig.3a), obtained from the GNSS data analysis. The $^{\delta v}/_{v}$ result shows a remarkable anticorrelation with both the δTWS and the IC1 time series. In the 2016-2017 time period a clear divergence of the $^{\delta v}/_{v}$ result with respect to the other two time series is well observable. It corresponds to the occurrence of the 2016 Central Italy seismic sequence, which has already been attested to cause seismic-velocity variations in the crust's elastic properties at regional scale by a similar noise-based study (Soldati et al., 2019).

As for the relatively smaller local seismic swarms, the strong imprint due to the hydrological perturbation in the area buries down any significant hint of the potential tectonic perturbation of the seismic episodes in the ATF region. In an attempt to enhance the perturbation signal potentially associated with the ATF- seismic swarms, we carried out a subtraction of the hydrological perturbation using the δTWS information. Literature describes elaborate methods on how to estimate the hydrological contribution from pluviometric observations: For instance, Illien et al. (2021) uses a model with coupling soil-water and groundwater dynamics, while Rivet et al. (2015) applies poroelastic relations based on pore-pressure diffusion and homogeneous hydraulic diffusivity. In our case, given that we have an estimate of the total water content in the medium, and observe a good similarity between both the $^{\delta v}/_{v}$ and the hydrological observations, we carry out the subtraction with the aid of a scaled δTWS obtained by linear robust regression, thus avoiding any further assumptions. After applying the hydrological correction in the $^{\delta v}/_{v}$ result the strong seasonal behaviour vanishes whereas the identification of perturbations related to the ATF-swarms remains not visible at all (see Fig.5b).

The second set of results, obtained from multiple consecutive narrow- frequency bands, allowed us to explore the perturbation response in the medium at the study site in multiple depth-sampling ranges (Hobiger et al., 2012). Fig.6 shows the corresponding $^{\delta v}/_{v}$ results from each of the six frequency bands analyzed, with respect to the time response of IC1 and the δTWS result. In these results we observe that the seasonal behaviour of the seismic-velocity perturbations decreases as we lower the frequency-content, but always remains present nonetheless. The resemblance between the δTWS and the $^{\delta v}/_{v}$ results with the higher frequency content (Figs.6a, 6b and 6c) is indicated in their corresponding Pearson's correlation coefficients: -0.71, -0.82 and -0.69, respectively. This is expected since the crustal depth-sampling range gets shallower, and thus more exposed to effects from perturbations due to surface/hydrological phenomena. Also, the top frequency-band results bear a foreseeable time delay (~15 d as estimated by cross-correlating the two time series) with respect to the δTWS, produced by the cross-correlation 30-day stacking bias. However, in the lowest frequency-band $^{\delta v}/_{v}$ results (Fig.6e and 6f) their low correlation coefficient (-0.47 and -0.44, respectively) show a weaker effect of the yearly seasonality, hence revealing the diminishing effect of hydrological perturbations as we sample deeper the scattering wavefield in the crust.

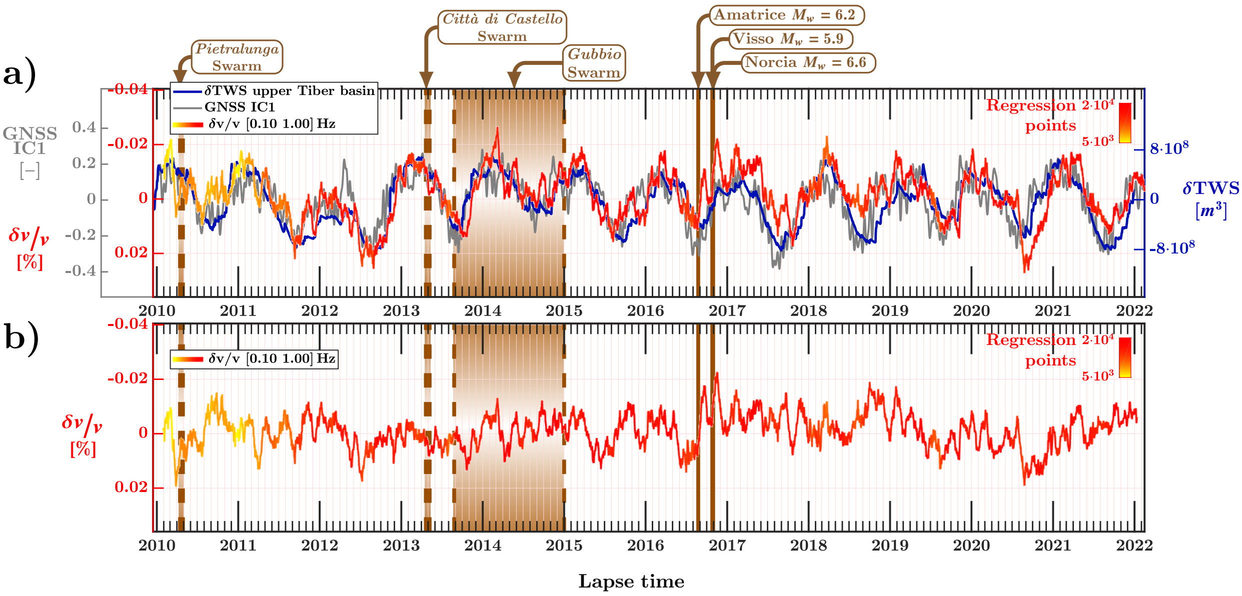

Figure 5: Comparison of geodetic (GNSS IC1) and hydrological (δTWS) observations with the relative seismic-velocity variations ($^{\delta v}/_{v}$), the latter displayed with reversed abscissa. Brown lines depict the bounds of the occurrence periods of the ATF seismic swarms (dashed) and the mainshock occurrences of the seismic sequence of Central Italy (solid). **a)** $^{\delta v}/_{v}$ result obtained from the complete frequency band [0.1 1.0] Hz, compared to the δTWS and the IC1 time response. **b)** Same $^{\delta v}/_{v}$ result in a) after applying a hydrological correction based on the δTWS result.

This detail indicates that seismic-velocity perturbations at depths larger than 3 km seem to be driven by phenomena other than surface hydrology.

In order to constrain the depth range of the results in Fig.6, we create a series of 1-D models that account for the depth characteristics of the mechanical properties of the study site. From the catalogue of oil-exploration activities carried out in the area (Progetto ViDEPI, 2009-2023) we select the boreholes with best logging completeness and largest depth reach (>2.5 km), and build five different 1-D geological models. We utilize the logging data to describe the elastic properties in depth and complete the missing information with values obtained from literature (Ciccotti et al., 2004; Trippetta et al., 2010; Ji et al., 2018; Chicco et al., 2019; Montone & Mariucci, 2020). We use the 1-D elastic models to calculate the fundamental-mode depth-sensitivity kernels of Rayleigh-wave phase velocity in order to observe the depth range where each of the frequency-band results is dominant (Herrmann, 2013). The depth-sensitivity kernels from the corresponding frequency bands of analysis are shown in Fig.7a for each of the locations, with the 1-D geological model of the corresponding borehole displayed in the background. Both $^{\delta v}/_{v}$ results in Fig.6 and depth-sensitivity curves in Fig.7a share the same color code by frequency band.Only depth-sensitivity kernels with respect to shear-wave velocity (β) perturbations are shown. Fig.7b depicts the dispersion curve of the Rayleigh-wave fundamental mode in the *Monte Civitello* 1-D model (based on the "Monte Civitello 001" borehole, Fig.7a) with respect to the six frequency bands of analysis, while Fig.7c shows the map distribution of the selected boreholes.

The use of multiple models serve to account for the varying depth sensitivity given the extension and geological complexity of this sector of the Apennines (see Figs.1a and

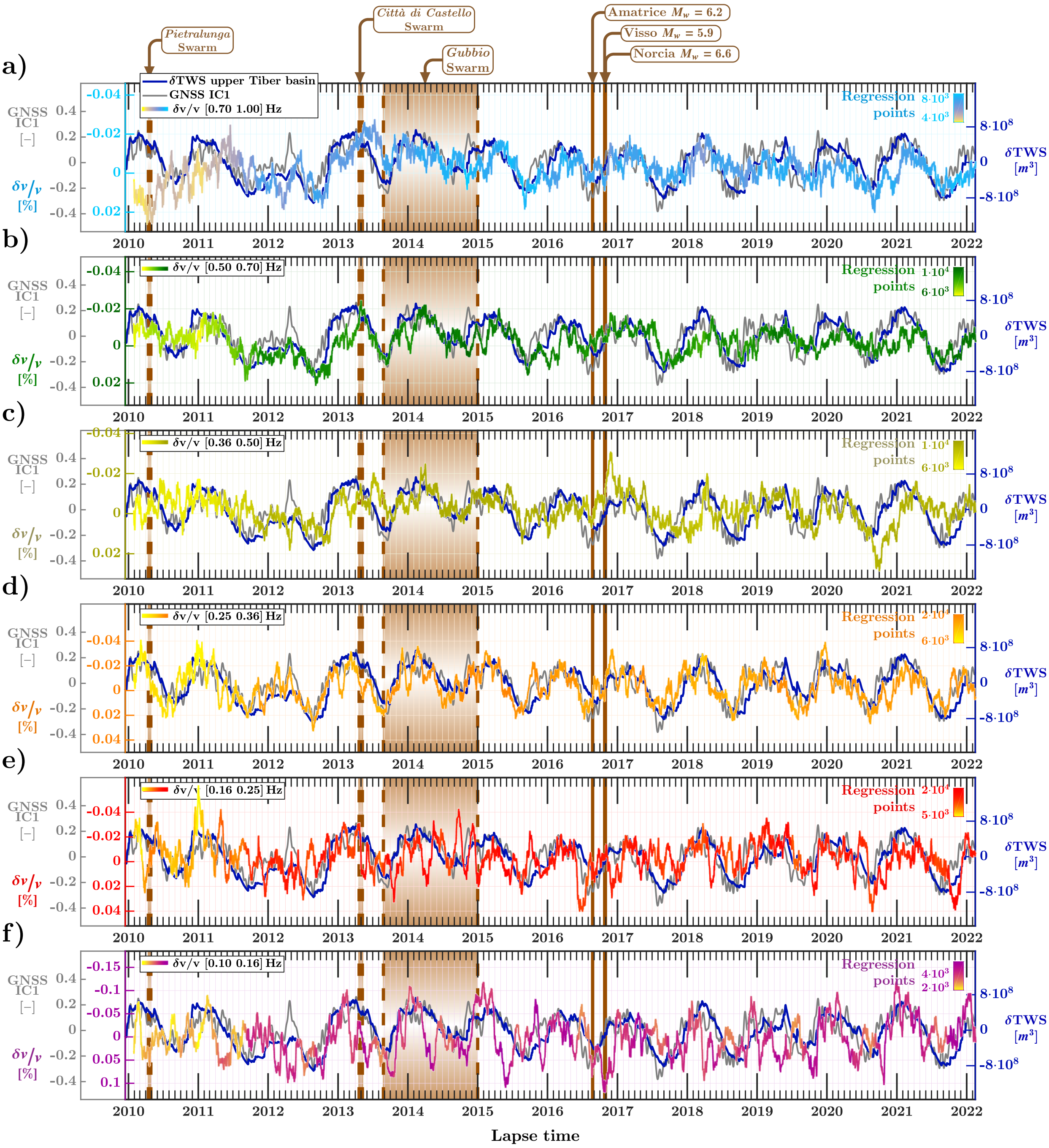

Figure 6: Comparison of GNSS IC1 time response, δTWS and $^{\delta v}/_{v}$ (abscissa-reversed) for different frequency bands: **a)** [0.7 1.0] Hz. **b)** [0.5 0.7] Hz. **c)** [0.35 0.5] Hz. **d)** [0.24 0.35] Hz. **e)** [0.16 0.24] Hz. **f)** [0.1 0.16] Hz. Brown lines represent the bounds of the occurrence periods of the ATF seismic swarms (dashed lines and shadowed region) and the mainshock occurrences of the seismic sequence of Central Italy (solid).

Fig.7c). Following this, the "San Donato 001" borehole represents the depth sensitivity of Rayleigh waves in the western area of the study site, in a model with shallow siliciclastic sequences and thick levels of the Burano formation. To the North, the

"Pieve S.Stefano 001" borehole provides a model with larger siliciclastic sequences and repeated carbonatic sequences in depth. The "Burano 001" and "Fossombrone 002" boreholes depict the thrust-and-fold complexity in the East and South of the study site: their corresponding graphs describe the Rayleigh-wave sensitivity when the medium is characterized by massive (duplexed-) carbonatic sequences of larger extension in depth. The borehole "Monte Civitello 001" provides a model of the central section of the study site, with a thick display of the Umbro-Marchigian formation and the complete carbonatic series in a single sequence.

For our final monitoring analysis, we make use of the elastic 1-D models and integrate all our multiple frequency-band results in order to estimate a depth distribution of the elastic-properties' perturbation that can describe the observed relative seismic-velocity variations at their respective frequency-band ranges. We implement the methodology for inversion of surface-wave dispersion curves (Dorman & Ewing, 1962; Szelwis & Behle, 1984; Socco & Strobbia, 2004) and adapt it to produce a depth-image result of the crustal perturbations observed in our ${}^{\delta v}/_{v}$ results at every lapse time. The description of the elastic properties in the 1-D models in Fig.7a enables the estimation of the (fundamental-mode) phase-velocity function for a laterally homogeneous medium with respect to the frequency values described within the depth limits of the model (see Fig.7b). Associating the multiple frequency-dependent ${}^{\delta v}/_{v}$ with the phase-velocity function we can constrain the physical magnitude of the phase-velocity perturbation δv for every frequency band at every lapse time. With the magnitude estimate of the phase-velocity change, we employ the depth-sensitivity kernels in Fig.7a to calculate the perturbation of the elastic properties of the medium. Since shear-wave velocity dominates propagation properties of Rayleigh waves (Xia et al., 1999; Louie, 2001; Wathelet et al., 2004), and assuming no mass-density changes happen in the medium, in this analysis we assume the crustal perturbations to be caused by shear-modulus changes ($\delta\mu$). In our approach, although the medium is simplified by assuming a stratified 1-D inhomogeneous half space, we disregard the retrieval of Rayleigh-wave higher-mode waveforms in our cross-correlation scattering coda given the geological complexity of the subsurface across the area and the strong variability of the geological structure (see Fig.7a) for the frequency range of our study. Hence, we neglect in our analysis any effect caused by the presence of cross-mode cross-correlation artefacts in our scattering coda (Kimman & Trampert, 2010). In our analysis the scattering is assumed to be controlled exclusively by the Rayleigh-wave fundamental mode and hence we neglect any Rayleigh-to-Rayleigh and Love-to-Rayleigh scattering mode conversions in the retrieved cross-correlation coda (Snieder, 1986). The depth-sensitivity kernels employed are originally conceived for Rayleigh-wave direct-arrival analysis and do not account for surface- to body-wave mode conversions (Chang & Tuan, 1973; Tuan, 1975; Momoi, 1981). Yet, Rayleigh-to-Rayleigh scattering mode becomes dominant with time because of their weaker decay (Maeda et al., 2008). Since our analysis mostly comprises late coda arrivals, and due to the fact that Rayleigh-to-Rayleigh scattering mode has a weaker decay (t^{-1}) with respect to the Rayleigh-to-body wave mode (t^{-4}), we neglect any scattering body-wave conversion and run under the premise that the analyzed coda is dominated by scattered Rayleigh waves.

For the inversion process we apply regularized damped least-squares (Tarantola & Valette, 1982; Haney & Tsai, 2017), employing the error estimate at each ${}^{\delta v}/_{v}$ regression result in order to build the diagonal data-covariance matrix. Although we counted on six frequency-band results, given the ill-posedness of our problem we employ 20 frequency samples, implying a repetitive use of the ${}^{\delta v}/_{v}$ time series but with varying amplitude, following the corresponding 1D model phase-velocity curve (see Fig.7b).

The final result we produce is a depth-monitoring image: a time-lapse with the depth distribution of crustal perturbations detected by our seismic stations assuming a laterally invariant medium, with isotropic scattering properties, and thus neglecting lateral

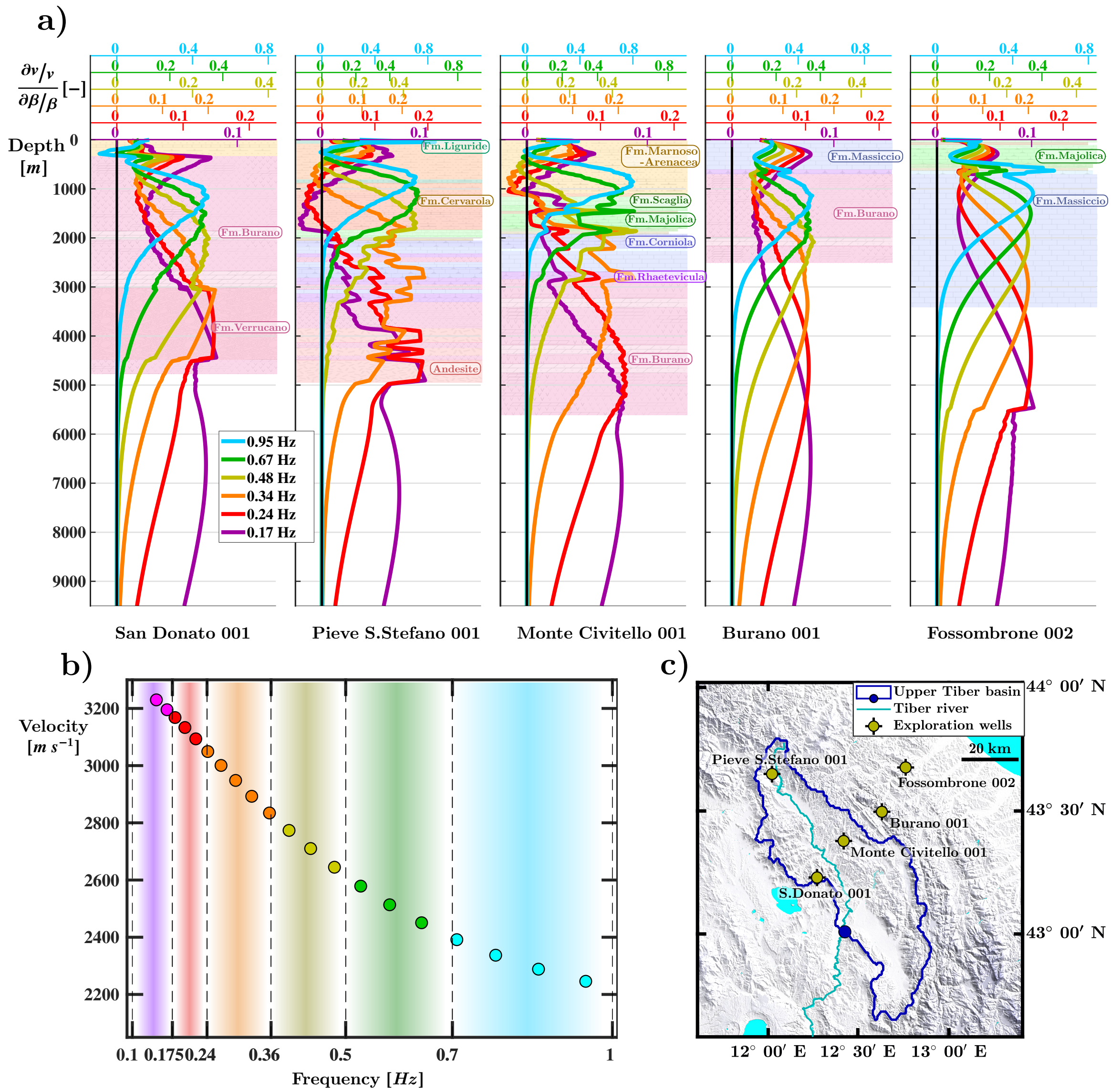

Figure 7: Depth sensitivity analysis: **a)** Fundamental-mode Rayleigh-wave depth-sensitivity kernels from five different 1-D geological models. Top colored axes define the amplitude values of their corresponding color-matching kernel. Main geological formations are named with colored labels. The geological models are based on the logging results of the respective boreholes, named at the bottom of their respective figure. The depth-sensitivity kernels correspond to phase-velocity sensitivity with respect to a perturbation in the shear-wave velocity (β), at the six frequency bands analyzed (see matching-color correspondence with results in Fig.6). **b)** Phase-velocity samples employed for the depth-monitoring imaging. Phase velocity values of the fundamental-mode Rayleigh wave for the *Monte Civitello* 1-D model in a). The colour of each frequency sample indicates to which of the 6 analyzed frequency bands it corresponds, and in turn which $^{\delta v}/_{v}$ time series in Fig.6 is employed during the depth-monitoring imaging process. **c)** Location of the boreholes from which the 1-D elastic models in a) were built.

perturbation-distributions. This sort of monitoring result has recently been presented in Fokker et al. (2023), where they adapt their depth-sensitivity kernels to retrieve the depth distribution of hydrologically-induced seismic perturbations in the form of pore-pressure variations.

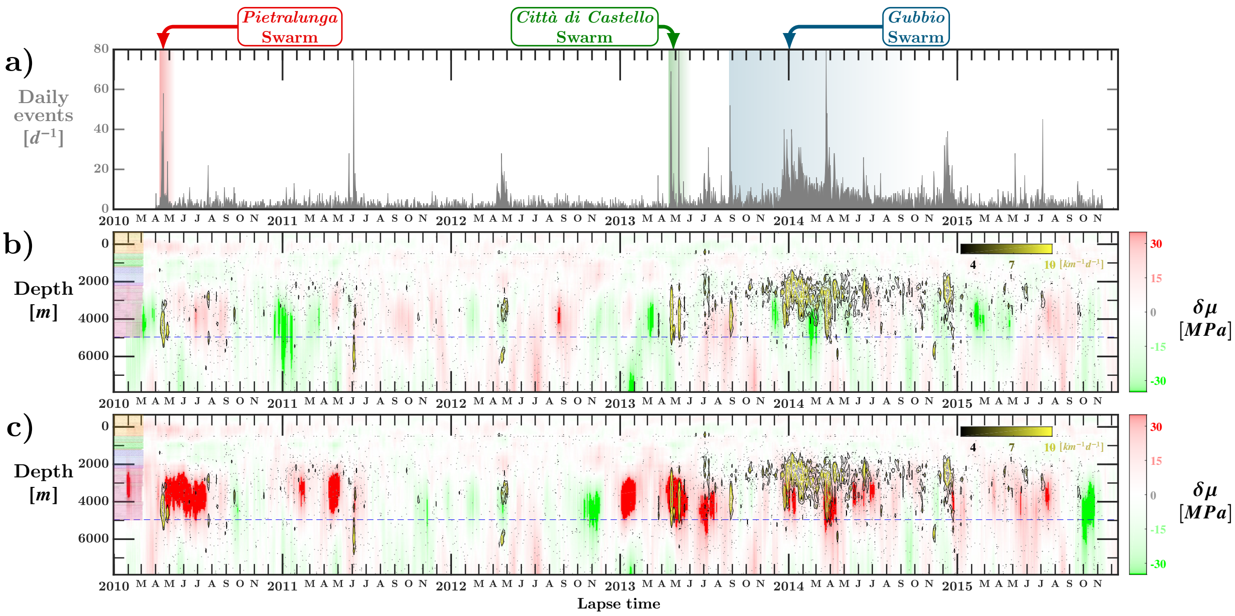

Figure 8: Depth-imaging monitoring of shear-modulus changes ($\delta\mu$) compared with the depth distribution of the seismic events in the ATF zone. Depth model is based on the "Monte Civitello 001" borehole (see Fig.7a). **a)** Daily number of seismic events with magnitude greater than the completeness magnitude ($M_L > 0.5$) in the ATF zone, as in the catalogue shown in Fig.1b. **b)** Monitoring of the crustal shear-modulus perturbation in depth from the multiple frequency-band $^{\delta v}/_{v}$ results. Seismic events in a) are displayed as individual dots and as a contour-density map in time and depth (color magnitudes in events per day and kilometer). Dashed blue line represents the limit of the "Monte Civitello 001" borehole. **c)** Same as in b), after applying the correction of the hydrologically induced perturbations with the aid of the Total Water Storage variation (δTWS) estimate.

Fig.8a shows the daily occurrence of seismic events from the seismic catalogue depicted in Fig.1b with magnitude greater than the completeness magnitude ($M_L > 0.5$, Pastoressa et al., 2023). The depth-imaging monitoring results displayed in Fig.8b and Fig.8c correspond to the use of the *Monte Civitello* 1-D model. Results are displayed in depth using the mean sea level as permanent datum and the measured depth has been shifted with respect to the "Monte Civitello 001" drill floor. The dashed blue line depicts the limit of the borehole in depth, which means that the model becomes homogeneous beyond this limit. The depth versus time of the complete catalogue (i.e., only seismic events with $M_L > 0.5$) is superimposed.

Without applying any hydrological correction, the depth-imaging monitoring shows that the shear-modulus perturbations happen independently from the time occurrence of seismic events (Fig.8b). On the other hand, Fig.8c shows the result of applying the same inversion technique on the multiple frequency-dependent relative seismic-velocity variation results after applying an individually-customized δTWS-based correction of the hydrological seismic perturbation on each $^{\delta v}/_{v}$ time series (sane correction applied in the $^{\delta v}/_{v}$ result of Fig.5b). In these results one can easily identify blunt increases in the medium's shear modulus at the occurrence time of seismic swarms, in the range of tens of MPa and always within the seismogenic depth range (roughly between 2 and 5 km of depth). At the same time of the *Pietralunga* swarm, an increase of $\delta\mu$ sustained in time for 3 months is observed; high density seismic occurrences in the first half of 2011 coincide with short duration crustal shear-modulus perturbations. The second half of 2011 and the whole 2012 show a time interval of small perturbations concurring with a period of seismic quiescence. Then, an increase of crustal shear-modulus perturbation occurs in January 2013 (no seismic activity has been recorded at this time), and in April-May 2013 with the *Città di Castello* swarm occurrence. During the *Gubbio* seismic swarm $\delta\mu$ shows a first perturbation coinciding with the maximum magnitude event in December, 2013, followed by a larger and longer perturbation corresponding to the second peak of events in March-April, 2014. Later perturbation episodes during 2014 and 2015 match with seismic occurrences of smaller time concentration.

4 Discussion

We use the δTWS, the displacement associated with hydrological loading (HL) and the mean piezometric level (MPL) for the period 2010-2022 in order to get three independent observations related to temporal variations in water content of the shallow crust. The MPL, although showing a similar trend with the HL and the δTWS, displays a 30 d delay with respect to the latter two, but a good agreement and reduced time lag with IC4 from GNSS decomposition. These last two time series may be representative of possible local effects related with the southernmost region of the upper Tiber basin where most of the piezometric wells are located (Fig.2c) and also the GNSS stations show the maximum (vertical) displacements associated with IC4 (Fig.3).

Total water content variations are known to cause measurable ground deformations (from GNSS data analysis) but also affect the elastic parameters of the superficial crustal sections (from noise-based monitoring analysis). In the ATF area, if from one side the hydrological perturbations seem to be responsible for two independent components out of the four produced by the variational Bayesian ICA decomposition of GNSS time responses, its influence on perturbation of elastic parameters is still visible up to the first few km of depth (in the ${}^{\delta v}/_{v}$ results at frequency ranges from 0.25 to 1 Hz). Regarding the first point, this means that the TWS variations are the most important source of seasonal modulation of crustal deformation (~18% of data variance explained compared to the 14% of the seismic activity components as from Fig.3). Similarly, a relevant influence of δTWS arises from the ${}^{\delta v}/_{v}$ temporal variations of Fig.5 where the two time series show a very good anticorrelation (correlation coefficient of -0.81) and limited time lag (ca. ~4 d). Interestingly, this relationship holds also for most of the six shorter frequency bands (Fig.6). In particular we can observe a good anticorrelation (correlation coefficient < -0.5) for the higher frequency bands down to the fourth one [0.25 0.35] Hz. While for the two lower frequency bands (i.e., [0.1 0.17] and [0.17 0.25] Hz), i.e., the deepest portions of the crustal volume investigated, the periodic behavior associated with the δTWS is not visible anymore. By looking at the depth-sensitivity kernels of Fig. 7a we observe that these last two frequency range waves (red and magenta lines) are sampling deeper levels of the Earth's crust (roughly from 4 km depth further down for all crustal-structure models from all borehole locations), compared to the higher frequencies that are sensitive to the first 2-4 km of depth from the surface. Therefore we observe an influence of the TWS variations on the relative seismic-velocity variations in the crust until a depth of few km as already found also in other areas (Poli et al., 2020; Barajas et al., 2021; Almagro Vidal et al., 2021), thus indicating this observation as a possible general feature from the Southern and Central Apennines to the Alpine regions. Beside the δTWS influence, we could also observe that the co- and post-seismic variations associated with the 2016 Central Italy seismic sequence are mainly visible only in the two middle frequency ranges ([0.25 0.35] and [0.35 0.5] Hz), roughly corresponding to a depth range of 2-4 km. This may be explained by the presence of a CO_2 highly pressurized crustal level (Chiodini et al., 2004; Carannante et al., 2013), which may be able to amplify the effect of the shaking (as similarly seen also in Brenguier et al., 2014).

The strong influence of water content variations is easily separated from other sources of crustal perturbation in the GNSS data by applying variational Bayesian IC analysis (see Fig.3). For the relative seismic-velocity variations instead, the removal of the δTWS influence does not provide clear information on other possible sources of seismic perturbations, at least none clearly related to seismic swarm occurrences (Fig.5b). In order to improve exposure of the perturbations, we apply an inversion approach integrating the six frequency-band ${}^{\delta v}/_{v}$ results with the aid of their depth sensitivity and local 1-D elastic models of the crustal structure in depth. This procedure provides the monitoring of the crustal perturbations expressed in the form of shear-modulus variations and depicted as a depth distribution (Fig.8). In this case the removal of the hydrologically-induced seismic perturbation is carried out before inversion for each of the six $\delta v/v$ time series individually, with an independent scaling based on the similarity of each frequency-band $\delta v/v$ result with the δTWS. The final result unveils crustal shear-modulus perturbations displaying some comformity with the occurrence time and seismogenic depth of the ATF seismic swarms (Fig.8c). Our results describe an increase of crustal $\delta\mu$ concurrent with the seismic swarms, which is interpreted as the result of an increase in the compliance of the rock's pore space following a decrease in pore pressure (Freund, 1992; Khaksar et al., 2001; Shapiro, 2003). This is contrary to the main earthquake-generator process considered by the vast majority of research work in the region: the increase in pore pressure leading to a decrease of the effective stress on the fault plane, thus favoring the rupture (Rice, 1992; Axen, 1992; Miller et al., 1996). In agreement with this interpretation, a recent study also based on $\delta v/v$ analysis depicts a seismic-velocity decrease during the activity period of the *Città di Castello* and *Gubbio* swarms (Mikhael et al., 2024). Although they account for the perturbation effect produced by meteoclimatic phenomena in their analysis, the use of auto-correlation instead of cross-correlation, and the different frequency range and stacking-length employed makes the result comparison unsuitable.

The presence of overpressurized fluids in the upper crustal section (from few to 15 km of depth) under the Apennine belt has been extensively referred to as a primary source of instability and possibly the major triggering mechanism for the seismicity of this area (Chiodini et al., 2004), especially for the 1997-1998 Umbria-Marche seismic sequence (Quattrocchi, 1999; Chiarabba et al., 2009; Miller et al., 2004). Fluid circulation within the fault zone favours the replacement of strong minerals in the fault gouge which lead to frictional instabilities or fault weakening (Collettini et al., 2019; Volpe et al., 2022). This is expected at large depths, that explain the presence of the Alto Tiberina fault (Chiaraluce et al., 2007; Hreinsdóttir & Bennett, 2009; Vadacca et al., 2016), yet our observations refer to the normal-fault splay distributed in the ATF's hanging wall, at shallower levels. The sign of the crustal perturbations observed in our noise-based monitoring and its correlation with the seismic-swarm occurrences, however, reveal that the earthquake nucleation process might require further discussion, and could shed light on an alternative physical interpretation. Local seismic tomography imaging has revealed high pore-pressure conditions in depth (from 3 km, Piana Agostinetti et al., 2017; Chiarabba et al., 2020), which are confirmed by in situ readings of CO_2 pressure in deep exploration boreholes ("Pieve S.Stefano 001", "San Donato 001"). The observed increase in shear modulus in our results shows the fault rupture to be apparently driven by the poroelastic stress path defined by the pore-pressure relaxation following crustal CO_2 degassing. Some studies have referred to the fluid migration originating from mainshocks and their corresponding pore-pressure relaxation as the trigger to aftershock seismicity (Miller et al., 2004; Antonioli et al., 2005). Dahm & Fischer (2014) monitor changes on the V_P/V_s ratio on three mid-crustal swarms in NW-Bohemia over a 10 year span and identify abrupt decreases of the body-wave velocity ratio at the source region before and during the main seismic activity. They explained this observation as due to the degassing process of overpressurized fluids during the beginning phase of the swarm activity. Although we observe our perturbations in the form of shear-modulus increases, the former observation becomes similar to our $\delta\mu$ increase considering that the sensitivity kernels used in the inversion are based on shear-wave velocity changes. Moreover, within the Central Italy sequence, Chiarabba et al. (2020b) distinguished a precursory increase in body-wave velocity prior to the Norcia mainshock followed by an abrupt decrease at the time of rupture. Pore-pressure relaxation induces changes in the horizontal stress field, increases effective stress (A. Chan & Zoback, 2002; Zoback & Zinke, 2002) and defines stress paths that induce reactivation faulting (Hillis, 2000; Hettema, 2020; Van den Bogert & van Eijs, 2020). In future works we intend to confirm the increase in the crustal shear modulus associated with CO_2-degassing episodes by comparing our new results with recently available continuous CO_2-flux measurements in the field.

5 Conclusions

We have successfully integrated seismological, geodetic and hydrological observations in a multidisciplinary framework to monitor the deformation and changes in mechanical properties of the crust in the ATF zone. Our study identifies and quantifies the perturbation effect in the crust produced by surface phenomena and seismic activity, confirming the strong effect that surface hydrology plays in the monitoring results. The analysis of GNSS position time series with blind source separation highlights seasonal deformation signals associated with changes in water storage and surface hydrology and transient deformation signals associated with tectonic events.

We find that hydrologically-induced seismic perturbations are dominant in the ${}^{\delta v}/_{v}$ results from ambient seismic noise, masking weaker signals associated with minor tectonic events, such as low energy seismic swarms. If from one side, ambient seismic noise recordings successfully enable the continuous monitoring of the hydrological changes, estimates of the total water storage variation can be used as a proxy for the hydrologically-induced seismic perturbations in order to quantify its impact and hence apply its correction. Yet, even with this hydrological-effect correction the seismic perturbations related to the ATF seismic swarms remain unclear. The analysis of the ${}^{\delta v}/_{v}$ in reduced frequency bands can serve as an approach for detecting small-to-moderate-amplitude perturbations associated with low energy seismic swarms. By varying the frequency content, we analyze the seismic perturbations in consecutive overlapping depth ranges and get a better depth inspection of the crustal elastic-properties' variations caused by the local seismic swarms. The use of 1-D models based on well logging surveys can provide valuable information in the estimation of the penetration range of the seismic perturbations. Moreover, the estimation of the phase velocities based on the 1-D models facilitates an estimation of the magnitude of the seismic-velocity perturbation per frequency range. This estimate enables us to apply a perturbational inversion of the crustal changes, presented in the form of shear-modulus variations, and retrieve its distribution in depth at every lapse time. With the necessary correction for the hydrological-effect by means of the δTWS, this 1-D depth-monitoring imaging approach highlights seismic perturbations of the crustal properties that concur with the time of occurrence and depth range of the ATF seismic swarms. Our final results instill doubts on the manifold role of fluid migrations in the seismic swarms' generation processes in the Alto Tiberina Fault zone.

Data availability statement

Geodetic data provided by *Istituto Nazionale di Geofisica e Vulcanologia* (Serpelloni & Pintori, 2024), accessible at `https://zenodo.org/records/10809324`. Groundwater level data provided by (ARPA Umbria, 2006), available at `https://apps.arpa.umbria.it/acqua/contenuto/Livelli-Di-Falda`. Hydrological load model from (Dill & Dobslaw, 2013), dataset accessible at `http://rz-vm115.gfz-potsdam.de:8080/repository/entry/show?entryid=24aacdfe-f9b0-43b7-b4c4-bdbe51b6671b`. The precipitation, temperature, and river-flow data used to implement the hydrological model provided by (Servizio Idrografico Regione Umbria, 2021–2024), and available at `https://annali.regione.umbria.it/`, `https://www.sir.toscana.it/consistenza-rete`, `https://console.regione.marche.it/(http://app.protezionecivile.marche.it/sol/indexjs.sol?lang=it)`, for the regions of Umbria, Tuscany, and Marche, respectively. Extraterrestrial irradiance data accessible at `http://www.soda-pro.com/web-services/radiation/extraterrestrial-irradiance-and-toa`. Drainage direction maps used to define river basins available at `www.hydrosheds.org/page/availability`. Seismic data provided by *Istituto Nazionale di Geofisica e Vulcanologia* (INGV Seismological Data Centre, 2006), accessible at `https://eida.ingv.it/it/`.Well logs utilized to build the 1-D elastic models accessible at (Progetto ViDEPI, 2009-2023).

References

Almagro Vidal, C., Zaccarelli, L., Pintori, F., Bragato, P. L., & Serpelloni, E. (2021). Hydrological effects on seismic-noise monitoring in karstic media. *Geophysical Research Letters*, *48*(15), e2021GL093191. doi: 10.1029/2021GL093191

Andajani, R. D., Tsuji, T., Snieder, R., & Ikeda, T. (2020). Spatial and temporal influence of rainfall on crustal pore pressure based on seismic velocity monitoring. *Earth, Planets and Space*, *72*(1), 1–17. doi: 10.1186/s40623-020-01311-1

Anderlini, L., Serpelloni, E., & Belardinelli, M. E. (2016). Creep and locking of a low-angle normal fault: Insights from the Altotiberina fault in the Northern Apennines (Italy). *Geophysical Research Letters*, *43*(9), 4321–4329. doi: 10.1002/2016GL068604

Anggono, T., Nishimura, T., Sato, H., Ueda, H., & Ukawa, M. (2012). Spatio-temporal changes in seismic velocity associated with the 2000 activity of Miyakejima volcano as inferred from cross-correlation analyses of ambient noise. *Journal of volcanology and geothermal research*, *247*, 93–107. doi: 10.1016/j.jvolgeores.2012.08.001

Antonioli, A., Piccinini, D., Chiaraluce, L., & Cocco, M. (2005). Fluid flow and seismicity pattern: Evidence from the 1997 Umbria-Marche (central Italy) seismic sequence. *Geophysical Research Letters*, *32*(10). doi: 10.1029/2004GL022256

ARPA Umbria. (2006). *Agenzia Regionale per la Protezione Ambientale Umbria.* Sistema Nazionale per la Protezione dell'Ambiente. Retrieved from `https://apps.arpa.umbria.it/acqua/contenuto/Livelli-Di-Falda` (Last accessed: March 12, 2024)

Axen, G. J. (1992). Pore pressure, stress increase, and fault weakening in low-angle normal faulting. *Journal of Geophysical Research: Solid Earth*, *97*(B6), 8979–8991. doi: 10.1029/92JB00517

Barajas, A., Poli, P., d'Agostino, N., Margerin, L., & Campillo, M. (2021). Separation of poroelastic and elastic processes of an aquifer from tectonic phenomena using geodetic, seismic, and meteorological data in the Pollino region, Italy. *Geochemistry, Geophysics, Geosystems*, *22*(11), e2021GC009742. doi: 10.1029/2021GC009742

Bettinelli, P., Avouac, J.-P., Flouzat, M., Bollinger, L., Ramillien, G., Rajaure, S., & Sapkota, S. (2008). Seasonal variations of seismicity and geodetic strain in the Himalaya induced by surface hydrology. *Earth and Planetary Science Letters*, *266*(3-4), 332–344. doi: 10.1016/j.epsl.2007.11.021

Blewitt, G., Kreemer, C., Hammond, W. C., & Gazeaux, J. (2016). MIDAS robust trend estimator for accurate GPS station velocities without step detection. *Journal of Geophysical Research: Solid Earth*, *121*(3), 2054–2068. doi: 10.1002/2015JB012552

Brenguier, F., Campillo, M., Hadziioannou, C., Shapiro, N., Nadeau, R., & Larose, E. (2008). Postseismic relaxation along the San Andreas Fault at Parkfield from continuous seismological observations. *Science*, *321*(5895), 1478–1481. doi: 10.1126/science.1160943

Brenguier, F., Campillo, M., Takeda, T., Aoki, Y., Shapiro, N., Briand, X., ... Miyake, H. (2014). Mapping pressurized volcanic fluids from induced crustal seismic velocity drops. *Science*, *345*(6192), 80–82. doi: 10.1126/science.1254073

Brenguier, F., Shapiro, N., Campillo, M., Ferrazzini, V., Duputel, Z., Coutant, O., & Nercessian, A. (2008). Towards forecasting volcanic eruptions using seismic noise. *Nature Geoscience*, *1*(2), 126–130. doi: 10.1038/ngeo104

Budi-Santoso, A., & Lesage, P. (2016). Velocity variations associated with the large 2010 eruption of Merapi volcano, Java, retrieved from seismic multiplets and ambient noise cross-correlation. *Geophysical Journal International*, *206*(1), 221–240. doi: 10.1093/gji/ggw145

Campillo, M. (2006). Phase and correlation in 'random' seismic fields and the reconstruction of the Green function. *Pure and applied geophysics*, *163*, 475–502. doi: 10.1007/s00024-005-0032-8

Carannante, S., Monachesi, G., Cattaneo, M., Amato, A., & Chiarabba, C. (2013). Deep structure and tectonics of the Northern-Central Apennines as seen by regional-scale tomography and 3-D located earthquakes. *Journal of Geophysical Research: Solid Earth*, *118*(10), 5391–5403. doi: 10.1002/jgrb.50371

Chan, A., & Zoback, M. (2002). Deformation analysis in reservoir space (DARS): a simple formalism for prediction of reservoir deformation with depletion. In *SPE/ISRM Rock Mechanics Conference.* Society of Petroleum Engineers. doi: 10.2118/78174-MS

Chan, K., Lee, T.-W., & Sejnowski, T. J. (2003). Variational Bayesian learning of ICA with missing data. *Neural Computation*, *15*(8), 1991–2011. doi: 10.1162/08997660360675116

Chang, C., & Tuan, H. (1973). On the surface-to-bulk mode conversion of Rayleigh waves. *IEEE Transactions on Microwave Theory and Techniques*, *21*, 558–560. doi: 10.1109/TMTT.1973.1128060

Chiarabba, C., Buttinelli, M., Cattaneo, M., & De Gori, P. (2020). Large earthquakes driven by fluid overpressure: The Apennines normal faulting system case. *Tectonics*, *39*(4), e2019TC006014. doi: 10.1029/2019TC006014

Chiarabba, C., De Gori, P., & Boschi, E. (2009). Pore-pressure migration along a normal-fault system resolved by time-repeated seismic tomography. *Geology*, *37*(1), 67–70. doi: 10.1130/G25220A.1

Chiarabba, C., De Gori, P., Segou, M., & Cattaneo, M. (2020b). Seismic velocity precursors to the 2016 Mw 6.5 Norcia (Italy) earthquake. *Geology*, *48*(9), 924–928. doi: 10.1130/G47048.1

Chiaraluce, L., Amato, A., Carannante, S., Castelli, V., Cattaneo, M., Cocco, M., ... others (2014). The Alto Tiberina Near Fault Observatory (Northern Apennines, Italy). *Annals of Geophysics*, *57*(3), S0327. doi: 10.4401/ag-6426

Chiaraluce, L., Chiarabba, C., Collettini, C., Piccinini, D., & Cocco, M. (2007). Architecture and mechanics of an active low-angle normal fault: Alto Tiberina fault, Northern Apennines, Italy. *Journal of Geophysical Research: Solid Earth*, *112*(B10). doi: 10.1029/2007JB005015

Chicco, J., Verdoya, M., Giuli, G., & Invernizzi, C. (2019). Thermophysical properties and mineralogical composition of the Umbria-Marche carbonate succession (central Italy). *Geological Society of America Special Paper*(542), 59–67. doi: 10.1130/2019.2542(02)

Chiodini, G., Cardellini, C., Amato, A., Boschi, E., Caliro, S., Frondini, F., & Ventura, G. (2004). Carbon dioxide Earth degassing and seismogenesis in central and southern Italy. *Geophysical Research Letters*, *31*(7), L07615. doi: 10.1029/2004GL019480

Ciccotti, M., Almagro, R., & Mulargia, F. (2004). Static and dynamic moduli of the seismogenic layer in Italy. *Rock mechanics and rock engineering*, *37*, 229–238. doi: 10.1007/s00603-003-0019-7

Clements, T., & Denolle, M. A. (2018). Tracking groundwater levels using the ambient seismic field. *Geophysical Research Letters*, *45*(13), 6459–6465. doi: 10.1029/2018GL077706

Collettini, C., Tesei, T., Scuderi, M. M., Carpenter, B. M., & Viti, C. (2019). Beyond Byerlee friction, weak faults and implications for slip behavior. *Earth and Planetary Science Letters*, *519*, 245–263. doi: 10.1016/j.epsl.2019.05.011

D'Agostino, N., Silverii, F., Amoroso, O., Convertito, V., Fiorillo, F., Ventafridda, G., & Zollo, A. (2018). Crustal deformation and seismicity modulated by groundwater recharge of karst aquifers. *Geophysical Research Letters*, *45*(22), 12–253. doi: 10.1029/2018GL079794

Dahm, T., & Fischer, T. (2014). Velocity ratio variations in the source region of earthquake swarms in NW Bohemia obtained from arrival time double-differences. *Geophysical Journal International*, *196*(2), 957–970. doi: 10.1093/gji/ggt410

Dill, R. (2008). Hydrological model LSDM for operational Earth rotation and gravity field variations. *Scientific Technical Report 08/09*. doi: 11.2312/GFZ.b103-08095

Dill, R., & Dobslaw, H. (2013). Numerical simulations of global-scale high-resolution hydrological crustal deformations. *Journal of Geophysical Research: Solid Earth*, *118*(9), 5008–5017. doi: 0.1002/jgrb.50353

Dong, D., Fang, P., Bock, Y., Cheng, M., & Miyazaki, S. (2002). Anatomy of apparent seasonal variations from GPS-derived site position time series. *Journal of Geophysical Research: Solid Earth*, *107*(B4), ETG–9. doi: 10.1029/2001JB000573

Dorman, J., & Ewing, M. (1962). Numerical inversion of seismic surface wave dispersion data and crust-mantle structure in the New York-Pennsylvania area. *Journal of Geophysical Research*, *67*(13), 5227–5241. doi: 10.1029/JZ067i013p05227

ECMWF. (n.d.). *European Centre for Medium Range Weather Forecasts.* Retrieved from `https://https://www.ecmwf.int/` (Last accessed: March 12, 2024)

EPOS. (n.d.). *Near Fault Observatory (NFO).* Retrieved from `https://www.epos-eu.org/tcs/near-fault-observatories/data-services` (Last accessed: March 12, 2024)

Fokker, E., Ruigrok, E., Hawkins, R., & Trampert, J. (2021). Physics-based relationship for pore pressure and vertical stress monitoring using seismic velocity variations. *Remote Sensing*, *13*(14), 2684. doi: 10.3390/rs13142684

Fokker, E., Ruigrok, E., Hawkins, R., & Trampert, J. (2023). 4D physics-based pore pressure monitoring using passive image interferometry. *Geophysical Research Letters*, *50*(5), e2022GL101254. doi: 10.1029/2022GL101254

Freund, D. (1992). Ultrasonic compressional and shear velocities in dry clastic rocks as a function of porosity, clay content, and confining pressure. *Geophysical Journal International*, *108*(1), 125–135. doi: 10.1111/j.1365-246X.1992.tb00843.x

Grêt, A., Snieder, R., & Scales, J. (2006). Time-lapse monitoring of rock properties with coda wave interferometry. *Journal of Geophysical Research: Solid Earth*, *111*(B3). doi: 10.1029/2004JB003354

Gualandi, A., Nichele, C., Serpelloni, E., Chiaraluce, L., Anderlini, L., Latorre, D., . . . Avouac, J.-P. (2017). Aseismic deformation associated with an earthquake swarm in the Northern Apennines (Italy). *Geophysical Research Letters*, *44*(15), 7706–7714. doi: 10.1002/2017GL073687

Gualandi, A., Serpelloni, E., & Belardinelli, M. E. (2016). Blind source separation problem in GPS time series. *Journal of Geodesy*, *90*, 323–341. doi: 10.1007/s00190-015-0875-4

Haney, M. M., & Tsai, V. C. (2017). Perturbational and nonperturbational inversion of Rayleigh-wave velocities. *Geophysics*, *82*(3), F15–F28. doi: 10.1190/GEO2016-0397.1

Herrmann, R. B. (2013). Computer programs in seismology: An evolving tool for instruction and research. *Seismological Research Letters*, *84*(6), 1081–1088. doi: 10.1785/0220110096

Hettema, M. (2020). Analysis of mechanics of fault reactivation in depleting reservoirs. *International Journal of Rock Mechanics and Mining Sciences*, *129*, 104290. doi: 10.1016/j.ijrmms.2020.104290

Hillers, G., Campillo, M., Ben-Zion, Y., & Roux, P. (2014b). Seismic fault zone trapped noise. *Journal of Geophysical Research: Solid Earth*, *119*(7), 5786–5799. doi: 10.1002/2014JB011217

Hillers, G., Campillo, M., & Ma, K.-F. (2014). Seismic velocity variations at TCDP are controlled by MJO driven precipitation pattern and high fluid discharge properties. *Earth and Planetary Science Letters*, *391*, 121–127. doi: 10.1016/j.epsl.2014.01.040

Hillis, R. (2000). Pore pressure/stress coupling and its implications for seismicity. *Exploration Geophysics*, *31*(2), 448–454. doi: 10.1071/EG00448

Hobiger, M., Wegler, U., Shiomi, K., & Nakahara, H. (2012). Coseismic and postseismic elastic wave velocity variations caused by the 2008 Iwate-Miyagi Nairiku earthquake, Japan. *Journal of Geophysical Research: Solid Earth*, *117*(B9). doi: 10.1029/2012JB009402

Hreinsdóttir, S., & Bennett, R. A. (2009). Active aseismic creep on the Alto Tiberina low-angle normal fault, Italy. *Geology*, *37*(8), 683–686. doi: 10.1130/G30194A.1

Illien, L., Andermann, C., Sens-Schönfelder, C., Cook, K., Baidya, K., Adhikari, L., & Hovius, N. (2021). Subsurface moisture regulates himalayan groundwater storage and discharge. *AGU Advances*, *2*(2), e2021AV000398. doi: 10.1029/2021AV000398

Illien, L., Sens-Schönfelder, C., Andermann, C., Marc, O., Cook, K. L., Adhikari, L. B., & Hovius, N. (2022). Seismic velocity recovery in the subsurface: transient damage and groundwater drainage following the 2015 Gorkha earthquake, Nepal. *Journal of Geophysical Research: Solid Earth*, *127*(2), e2021JB023402. doi: 10.1029/2021JB023402

INGV Seismological Data Centre. (2006). *Rete Sismica Nazionale.* Italy: Istituto Nazionale di Geofisica e Vulcanologia (INGV). Retrieved from `http://iside.rm.ingv.it/instruments` (Last accessed: March 12, 2024) doi: 10.13127/SD/X0FXNH7QFY

Ji, S., Li, L., Motra, H. B., Wuttke, F., Sun, S., Michibayashi, K., & Salisbury, M. H. (2018). Poisson's ratio and auxetic properties of natural rocks. *Journal of Geophysical Research: Solid Earth*, *123*(2), 1161–1185. doi: 10.1002/2017JB014606

Khaksar, A., Griffiths, & McCann. (2001). Compressional-and shear-wave velocities as a function of confining stress in dry sandstones. *Geophysical Prospecting*, *47*(4), 487–508. doi: 10.1046/j.1365-2478.1999.00146.x

Kimman, W., & Trampert, J. (2010). Approximations in seismic interferometry and their effects on surface waves. *Geophysical Journal International*, *182*(1), 461–476. doi: 10.1111/j.1365-246X.2010.04632.x

Latorre, D., Mirabella, F., Chiaraluce, L., Trippetta, F., & Lomax, A. (2016). As-sessment of earthquake locations in 3-D deterministic velocity models: A case study from the Altotiberina Near Fault Observatory (Italy). *Journal of Geophysical Research: Solid Earth*, *121*(11), 8113–8135. doi: 10.1002/2016JB013170

Liu, C., Aslam, K., & Daub, E. (2020). Seismic velocity changes caused by water table fluctuation in the New Madrid seismic zone and Mississippi embayment. *Journal of Geophysical Research: Solid Earth*, *125*(8), e2020JB019524. doi: 10.1029/2020JB019524

Louie, J. N. (2001). Faster, better: shear-wave velocity to 100 meters depth from refraction microtremor arrays. *Bulletin of the Seismological Society of America*, *91*(2), 347–364. doi: 10.1785/0120000098

Maeda, T., Sato, H., & Nishimura, T. (2008). Synthesis of coda wave envelopes in randomly inhomogeneous elastic media in a half-space: single scattering model including Rayleigh waves. *Geophysical Journal International*, *172*(1), 130–154. doi: 10.1111/j.1365-246X.2007.03603.x

Mandler, E., Pintori, F., Gualandi, A., Anderlini, L., Serpelloni, E., & Belardinelli, M. E. (2021). Post-seismic deformation related to the 2016 Central Italy seismic sequence from GPS displacement time-series. *Journal of Geophysical Research: Solid Earth*, *126*(9), e2021JB022200. doi: 10.1029/2021JB022200

Meier, U., Shapiro, N. M., & Brenguier, F. (2010). Detecting seasonal variations in seismic velocities within Los Angeles basin from correlations of ambient seismic noise. *Geophysical Journal International*, *181*(2), 985–996. doi: 10.1111/j.1365-246X.2010.04550.x

Mikhael, N., Poli, P., & Garambois, S. (2024). Non-linear seismic velocity variations observed during a seismic swarm in the Alto Tiberina low angle normal fault from ambient noise correlation measurements. *Journal of Geophysical Research: Solid Earth*, *129*(2), e2023JB028232. doi: 10.1029/2023JB028232

Miller, S. A., Collettini, C., Chiaraluce, L., Cocco, M., Barchi, M., & Kaus, B. J. (2004). Aftershocks driven by a high-pressure CO_2source at depth. *Nature*, *427*(6976), 724–727. doi: 10.1038/nature02251

Miller, S. A., Nur, A., & Olgaard, D. L. (1996). Earthquakes as a coupled shear stress-high pore pressure dynamical system. *Geophysical Research Letters*, *23*(2), 197–200. doi: 10.1029/95GL03178

Minato, S., Tsuji, T., Ohmi, S., & Matsuoka, T. (2012). Monitoring seismic velocity change caused by the 2011 Tohoku-oki earthquake using ambient noise records. *Geophysical Research Letters*, *39*(9). doi: 10.1029/2012GL051405

Momoi, T. (1981). Scattering of Rayleigh wave at a vertical boundary. *Journal of Physics of the Earth*, *29*(5), 435–485. doi: 10.4294/jpe1952.29.435

Montone, P., & Mariucci, M. T. (2020). Constraints on the structure of the shallow crust in central Italy from geophysical log data. *Scientific reports*, *10*(1), 3834. doi: 10.1038/s41598-020-60855-0

Pan, Y., Chen, R., Ding, H., Xu, X., Zheng, G., Shen, W., … Li, S. (2019). Common mode component and its potential effect on GPS-inferred three-dimensional crustal deformations in the Eastern Tibetan Plateau. *Remote Sensing*, *11*(17), 1975. doi: 10.3390/rs11171975

Pastoressa, A. E., Murru, M., Taroni, M., Console, R., Montuori, C., Falcone, G., & Di Stefano, R. (2023). Temporal Variations of Seismicity Rates and Gutenberg–Richter b-Values for a Stochastic Declustered Catalog: An Example in Central Italy. *Seismological Society of America*(94), 1566–1578. doi: 10.1785/0220220298

Piana Agostinetti, N., Giacomuzzi, G., & Chiarabba, C. (2017). Seismic swarms and diffuse fracturing within Triassic evaporites fed by deep degassing along the low-angle Alto Tiberina normal fault (Central Apennines, Italy). *Journal of Geophysical Research: Solid Earth*, *122*(1), 308–331. doi: 10.1002/2016JB013295

Pintori, F., Serpelloni, E., & Gualandi, A. (2022). Common-mode signals and vertical velocities in the greater Alpine area from GNSS data. *Solid Earth*, *13*(10), 1541–1567. doi: 10.5194/se-13-1541-2022

Pintori, F., Serpelloni, E., Longuevergne, L., Garcia, A., Faenza, L., D'Alberto, L., … Belardinelli, M. E. (2021). Mechanical response of shallow crust to groundwater storage variations: Inferences from deformation and seismic observations in the Eastern Southern Alps, Italy. *Journal of Geophysical Research: Solid Earth*, *126*(2), e2020JB020586. doi: 10.1029/2020JB020586

Poli, P., Marguin, V., Wang, Q., D'Agostino, N., & Johnson, P. (2020). Seasonal and coseismic velocity variation in the region of L'Aquila from single station measurements and implications for crustal rheology. *Journal of Geophysical Research: Solid Earth*, *125*(7), e2019JB019316. doi: 10.1029/2019JB019316

Poupinet, G., Ellsworth, W., & Frechet, J. (1984). Monitoring velocity variations in the crust using earthquake doublets: An application to the Calaveras Fault, California. *Journal of Geophysical Research: Solid Earth*, *89*(B7), 5719–5731. doi: 10.1029/JB089iB07p05719

Progetto ViDEPI. (2009-2023). *Visibility of Petroleum Exploration Data in Italy.* Ministero dello sviluppo economico DGRME - Società Geologica Italiana - Assomineraria. Retrieved from `https://www.videpi.com/videpi/pozzi/regione.asp?ub=T`

Pushpalatha, R., Perrin, C., Le Moine, N., Mathevet, T., & Andréassian, V. (2011). A downward structural sensitivity analysis of hydrological models to improve low-flow simulation. *Journal of hydrology*, *411*(1-2), 66–76. doi: 10.1016/j.jhydrol.2011.09.034

Quattrocchi, F. (1999). In search of evidence of deep fluid discharges and pore pressure evolution in the crust to explain the seismicity style of the Umbria-Marche 1997-1998 seismic sequence (Central Italy). *Annali di Geofisica*, *42*(4), 609–636. Retrieved from `http://hdl.handle.net/2122/1398` doi: 10.4401/ag-3743

Rice, J. (1992). Fault stress states, pore pressure redistributions, and the Weakness of the San Andreas Fault. In *Fault Mechanics and Transport Properties of Rocks* (eds. Evans, B. & Wong, T.F.). , *51*, 475–503.

Riddell, A. R., King, M. A., & Watson, C. S. (2020). Present-day vertical land motion of Australia from GPS observations and geophysical models. *Journal of Geophysical Research: Solid Earth*, *125*(2), e2019JB018034. doi: 10.1029/2019JB018034

Rivet, D., Brenguier, F., & Cappa, F. (2015). Improved detection of preeruptive seismic velocity drops at the piton de la fournaise volcano. *Geophysical Research Letters*, *42*(15), 6332–6339. doi: 10.1002/2015GL064835

Rovida, A., Locati, M., Camassi, R., Lolli, B., & Gasperini, P. (2020). The Italian earthquake catalogue CPTI15. *Bulletin of Earthquake Engineering*, *18*(7), 2953–2984. doi: 10.1007/s10518-020-00818-y

Sens-Schönfelder, C., & Wegler, U. (2006). Passive image interferometry and seasonal variations of seismic velocities at Merapi volcano, Indonesia. *Geophysical research letters*, *33*(21). doi: 10.1029/2006GL027797

Serpelloni, E., Cavaliere, A., Martelli, L., Pintori, F., Anderlini, L., Borghi, A., … others (2022). Surface velocities and strain-rates in the Euro-Mediterranean region from massive GPS data processing. *Frontiers in Earth Science*. doi: 10.3389/feart.2022.907897

Serpelloni, E., Faccenna, C., Spada, G., Dong, D., & Williams, S. D. (2013). Vertical GPS ground motion rates in the Euro-Mediterranean region: New evidence of velocity gradients at different spatial scales along the Nubia-Eurasia plate boundary. *Journal of Geophysical Research: Solid Earth*, *118*(11), 6003–6024. doi: 10.1002/2013JB010102

Serpelloni, E., & Pintori, F. (2024). *Displacement time series from GNSS stations in the Alto Tiberina Fault area (Central Italy) [Data set].* Zenodo. Retrieved from `https://zenodo.org/records/10809324` doi: 10.5281/zenodo.10809324

Serpelloni, E., Pintori, F., Gualandi, A., Scoccimarro, E., Cavaliere, A., Anderlini, L., . . . Todesco, M. (2018). Hydrologically Induced Karst Deformation: Insights From GPS Measurements in the Adria-Eurasia Plate Boundary Zone. *Journal of Geophysical Research: Solid Earth*, *123*(5), 4413–4430. doi: 10.1002/2017JB015252

Servizio Idrografico Regione Umbria. (2021–2024). *Servizio Idrografico Regione Umbria.* Retrieved from https://annali.regione.umbria.it/ (Last accessed: March 12, 2024)

Shapiro, S. A. (2003). Elastic piezosensitivity of porous and fractured rocks. *Geophysics*, *68*(2), 482–486. doi: 10.1190/1.1567215

Silverii, F., d'Agostino, N., Métois, M., Fiorillo, F., & Ventafridda, G. (2016). Transient deformation of karst aquifers due to seasonal and multiyear groundwater variations observed by GPS in Southern Apennines (Italy). *Journal of Geophysical Research: Solid Earth*, *121*(11), 8315–8337. doi: 10.1002/2016JB013361

Snieder, R. (1986). 3-D linearized scattering of surface waves and a formalism for surface wave holography. *Geophysical Journal International*, *84*(3), 581–605. doi: 10.1111/j.1365-246X.1986.tb04372.x

Snieder, R. (2006). The theory of coda wave interferometry. *Pure and Applied geophysics*, *163*(2-3), 455–473. doi: 10.1007/s00024-005-0026-6

Snieder, R., Grêt, A., Douma, H., & Scales, J. (2002). Coda wave interferometry for estimating nonlinear behavior in seismic velocity. *Science*, *295*(5563), 2253–2255. doi: 10.1126/science.1070015

Socco, L., & Strobbia, C. (2004). Surface-wave method for near-surface characterization: A tutorial. *Near surface geophysics*, *2*(4), 165–185. doi: 10.3997/1873-0604.2004015

Soldati, G., Zaccarelli, L., & Faenza, L. (2019). Spatio-temporal seismic velocity variations associated to the 2016–2017 central Italy seismic sequence from noise cross-correlation. *Geophysical Journal International*, *219*(3), 2165–2173. doi: 10.1093/gji/ggz429

Szelwis, R., & Behle, A. (1984). Shear-wave velocity of the weathering zone from multimodal Rayleigh waves. In *Seg technical program expanded abstracts 1984* (pp. 721–723). Society of Exploration Geophysicists. doi: 10.1190/1.1894225

Tarantola, A., & Valette, B. (1982). Generalized nonlinear inverse problems solved using the least squares criterion. *Reviews of Geophysics*, *20*(2), 219–232. doi: 10.1029/RG020i002p00219

Trippetta, F., Collettini, C., Vinciguerra, S., & Meredith, P. (2010). Laboratory measurements of the physical properties of Triassic Evaporites from Central Italy and correlation with geophysical data. *Tectonophysics*, *492*(1-4), 121–132. doi: 10.1016/j.tecto.2010.06.001

Tsai, V. C. (2011). A model for seasonal changes in GPS positions and seismic wave speeds due to thermoelastic and hydrologic variations. *Journal of Geophysical Research: Solid Earth*, *116*(B4). doi: 10.1029/2010JB008156

Tuan, H.-S. (1975). On bulk waves excited at a groove by Rayleigh waves. *Journal of Applied Physics*, *46*(1), 36–41. doi: 10.1063/1.321345

Vadacca, L., Casarotti, E., Chiaraluce, L., & Cocco, M. (2016). On the mechanical behaviour of a low-angle normal fault: the Alto Tiberina fault (Northern Apennines, Italy) system case study. *Solid Earth*, *7*(6), 1537–1549. doi: 10.5194/se-7-1537-2016

Valoroso, L., Chiaraluce, L., Di Stefano, R., & Monachesi, G. (2017). Mixed-mode slip behavior of the Altotiberina low-angle normal fault system (Northern Apennines, Italy) through high-resolution earthquake locations and repeating events. *Journal of Geophysical Research: Solid Earth*, *122*(12), 10–220. doi: 10.1002/2017JB014607

Van den Bogert, P., & van Eijs, R. (2020). Why Mohr-circle analyses may underestimate the risk of fault reactivation in depleting reservoirs. *International Journal of Rock Mechanics and Mining Sciences*, *136*, 104502. doi: 10.1016/j.ijrmms.2020.104502

Voisin, C., Guzmán, M. A. R., Refloch, A., Taruselli, M., & Garambois, S. (2017). Groundwater monitoring with passive seismic interferometry. *Journal of Water Resource and Protection*, *9*(12), 1414–1427. doi: 10.4236/jwarp.2017.912091

Volpe, G., Pozzi, G., Carminati, E., Barchi, M. R., Scuderi, M. M., Tinti, E., ... Collettini, C. (2022). Frictional controls on the seismogenic zone: Insights from the Apenninic basement, Central Italy. *Earth and Planetary Science Letters*, *583*, 117444. doi: 10.1016/j.epsl.2022.117444

Vuan, A., Brondi, P., Sugan, M., Chiaraluce, L., Di Stefano, R., & Michele, M. (2020). Intermittent slip along the Alto Tiberina Low-Angle Normal Fault in Central Italy. *Geophysical Research Letters*, *47*(17), e2020GL089039. doi: 10.1029/2020GL089039

Wathelet, M., Jongmans, D., & Ohrnberger, M. (2004). Surface-wave inversion using a direct search algorithm and its application to ambient vibration measurements. *Near surface geophysics*, *2*(4), 211–221. doi: 10.3997/1873-0604.2004018

White, A. M., Gardner, W. P., Borsa, A. A., Argus, D. F., & Martens, H. R. (2022). A review of GNSS/GPS in hydrogeodesy: Hydrologic loading applications and their implications for water resource research. *Water Resources Research*, *58*(7), e2022WR032078. doi: 10.1029/2022WR032078

Xia, J., Miller, R. D., & Park, C. B. (1999). Estimation of near-surface shear-wave velocity by inversion of Rayleigh waves. *Geophysics*, *64*(3), 691–700. doi: 10.1190/1.1444578

Yates, A., Savage, M., Jolly, A., Caudron, C., & Hamling, I. (2019). Volcanic, co-seismic, and seasonal changes detected at White Island (Whakaari) volcano, New Zealand, using seismic ambient noise. *Geophysical Research Letters*, *46*(1), 99–108. doi: 10.1029/2018GL080580

Zaccarelli, L., Shapiro, N., Faenza, L., Soldati, G., & Michelini, A. (2011). Variations of crustal elastic properties during the 2009 L'Aquila earthquake inferred from cross-correlations of ambient seismic noise. *Geophysical research letters*, *38*(24). doi: 10.1029/2011GL049750

Zoback, M. D., & Zinke, J. C. (2002). Production-induced normal faulting in the Valhall and Ekofisk oil fields. *Pure and applied geophysics*, *159*(1), 403–420. doi: 10.1007/PL00001258

Crustal deformation and seismic velocity perturbations in the Alto Tiberina fault zone (Northern Apennines, Italy)

C. Almagro Vidal[1], L. Zaccarelli[1], F. Pintori[1], and E. Serpelloni[1]

[1]National Institute of Geophysics and Volcanology - INGV Bologna

Key Points:

- Crustal-perturbation monitoring
- Ambient seismic noise
- Hydrological and seismic perturbations

Abstract

Crustal perturbations related to seismic activity can generally be observed with the occurrence of a large magnitude event. For less energetic seismic sequences though, the associated transient crustal variations are questionably measurable, and their observation gets easily obscured by relatively stronger perturbations such as the ones related to hydrological processes. In this study we reveal the significant role that terrestrial water-storage variations play in governing temporal crustal changes in the tectonically active Northern Apennines of Italy, and discuss the potential of accounting for its correction in order to monitor the relatively weaker transient perturbations caused by local seismic swarms. This area is characterized by an extensive level of low-energetic seismic activity, typically clustered in time and space, of which three main seismic swarms outstand during the 12 year period of study (2010-2021). Our analysis compares independent observations and processing methods of GNSS measurements and ambient seismic noise recordings. We adopt a multivariate statistical approach to discriminate between independent sources of ground deformation, and seismic noise cross-correlation analysis to monitor relative seismic-velocity variations. The result shows how the perturbation effects produced by variations in total water content are dominant in both time series of ground deformations and seismic-velocity variations. After correcting for the water-related variation effects, our monitoring results reveal perturbations in the crustal properties whose activation time and depth range correlate with the occurrences of the seismic swarms.

Plain Language Summary

The observation of changes in the Earth's crust, either as surface ground deformation or perturbations in its elastic properties, is crucial in the study of the earthquake nucleation process. When the occurrence of seismic events involves small magnitudes, however, these observations become hardly visible and get easily masked by other relatively-larger crustal changes induced by surface phenomena such as the hydrological cycle. Geodetic-data processing achieves to estimate different ground deformation responses induced by independent phenomena, separating that due to seismic origin from the ones induced by the hydrological cycle. When monitoring the crustal properties with ambient seismic noise, the separation of the perturbation by their different sources becomes rather challenging. In the case of our study, a fast approach involves the estimation of the hydrological cycle, and use it as a proxy to correct for the hydrologically-induced perturbations. With this correction, we observe an agreement between the crustal elastic properties' changes with the occurrence of local seismic swarms both in time and depth.

1 Introduction

Seasonal variations are common in many geophysical monitoring datasets. Ground displacements, as recorded by Global Navigation Satellite System (GNSS) networks, respond to a variety of multiscale processes causing seasonal deformation signals (e.g., Dong et al., 2002), and the understanding of the mechanisms behind this periodic deformation has recently brought a vast amount of literature with it (White et al., 2022, and references therein). Seasonal changes in elastic properties of the Earth's crust, as obtained from the analysis of seismic noise cross-correlations, are also described in the most recent literature (e.g., Meier et al., 2010; Hillers et al., 2014; Poli et al., 2020; Andajani et al., 2020; Fokker et al., 2021). Moreover, seasonal changes in seismicity rates, as the response to seasonal stress changes at seismogenic depths, have been observed in several tectonic settings (Bettinelli et al., 2008; D'Agostino et al., 2018; Pintori et al., 2021). Accounting for these seasonal signals is mandatory in order to accurately estimate trends and their changes, and to detect transient signals associated with tectonic processes and the earthquake preparatory phase, particularly in slowly deforming regions, where tectonic transients may be much smaller in amplitude than non tectonic seasonal signals. GNSS time responses due to the latter are often associated with climatic and hydrological processes (e.g., Pan et al., 2019; Riddell et al., 2020; Pintori et al., 2022). Additionally, seasonal signals can bring important information on underlying processes, such as groundwater or surface-water changes, with important implications in either the monitoring of hydrological resources or measuring the mechanical properties of the Earth. Silverii et al. (2016) showed that hydrological-recharge and -discharge processes in karstic aquifers of the Southern and Central Apennines (Italy) can produce deformation signals of both seasonal and transient nature in GNSS position time series. The hydrologically-induced transient signals, which are recorded also by Serpelloni et al. (2018) in the Southern Alps, are important to recognize not only because they can be used as indirect indicators of groundwater content, but also because they can be misinterpreted as transient tectonic signals.

The use of ambient seismic noise cross-correlation analysis has gained popularity in seismology in the study and monitoring of the elastic properties of the Earth's subsurface. One effective method for monitoring changes with ambient seismic noise is the description of the perturbations in the medium in terms of relative seismic-velocity variations (Snieder et al., 2002; Grêt et al., 2006; Campillo, 2006). This method is mostly being employed in the detection of coseismic perturbations and post-seismic relaxation effects after strong seismic events (Brenguier et al., 2008; Zaccarelli et al., 2011; Minato et al., 2012), or in monitoring perturbations in volcanic areas (Brenguier et al., 2008; Anggono et al., 2012; Budi-Santoso & Lesage, 2016). Since the beginning of the application of this noise-based analysis, it has been clear how the water content in the Earth's crust plays an important role in determining the relative seismic-velocity variations (Sens-Schönfelder & Wegler, 2006; Tsai, 2011; Hillers et al., 2014b), and in recent years it has also been used to monitor hydrological perturbations (Voisin et al., 2017; Clements & Denolle, 2018; Yates et al., 2019; Liu et al., 2020; Illien et al., 2022).

In this work we discuss the results obtained from the analysis of GNSS position time-series, seismic-velocity perturbations and groundwater content in the Northern Apennines of Italy. We focus on the Alto Tiberina Fault (ATF) area (see Fig.1a), where multidisciplinary measurements are guaranteed by dense monitoring networks. Since 2010, a Near Fault Observatory has been created in order to monitor ground deformation and seismicity through a multidisciplinary infrastructure (with seismological, geodetic, and geochemical measurements, Chiaraluce et al., 2014; EPOS, n.d.). The study area is located in the high strain-rate belt that runs along the regional divide of the Italian Apennines (Anderlini et al., 2016; Serpelloni et al., 2022). The most important geological feature here is the Alto Tiberina fault, an active low-angle (dip angle of 15°) normal fault, NNW trending and about 60 km long (e.g., Chiaraluce et al., 2007). The ATF and its hanging-wall high-angle faults account for $\sim 2\,{}^{mm}/_{y}$ out of the $3\,{}^{mm}/_{y}$ regional extension rate across the Northern Apennines (Anderlini et al., 2016). Historical catalogues in the Umbria-Marche region document several earthquakes with macroseismic estimate of magnitudes greater than $M_w = 5.5$ being the largest one a $M_w = 6.4$ in 1781 (Rovida et al., 2020), yet no large earthquakes are unequivocally associated with the ATF. Geodetic measurements suggest that the ATF is aseismically creeping at depths greater than 5 km (Anderlini et al., 2016; Vadacca et al., 2016), where it is well delineated by microseismicity. More importantly, the same area experiences low-energetic seismic swarms confined in the shallower, hanging-wall faults (Gualandi et al., 2017) with possible involvement of the ATF (Vuan et al., 2020). During the 12 year period (2010-2021) of study, the ATF area has been interested by a sustained seismic activity whose occurrence may be grouped into three main swarms (after Valoroso et al., 2017):

1. the *Pietralunga* swarm from 10 April 2010 to 5 May 2010, with maximum $M_w = 3.6$;
2. the *Città di Castello* swarm from 20 April 2013 to 20 May 2013, with maximum $M_w = 3.6$;
3. the *Gubbio* swarm that started on 26 August 2013 and lasted until the end of 2014, with a maximum $M_w = 3.9$ on 22 December 2013.

Fig.1b shows the daily occurrence of the whole ATF seismicity from 2010 to 2015, while the map in Fig.1c depicts the epicentral location of events of the three aforementioned seismic swarms. Afterwards the local seismicity did not show additional clusters, which may be also masked by the 2016 Central Italy seismic sequence.

The goal of this study is to analyze the main source of crustal deformation and seismic-velocity variations in the area during the 12 year period of observations, trying to discriminate among the different possible sources of perturbations, from the water content variations to the tectonic activity occurred up to 2015.

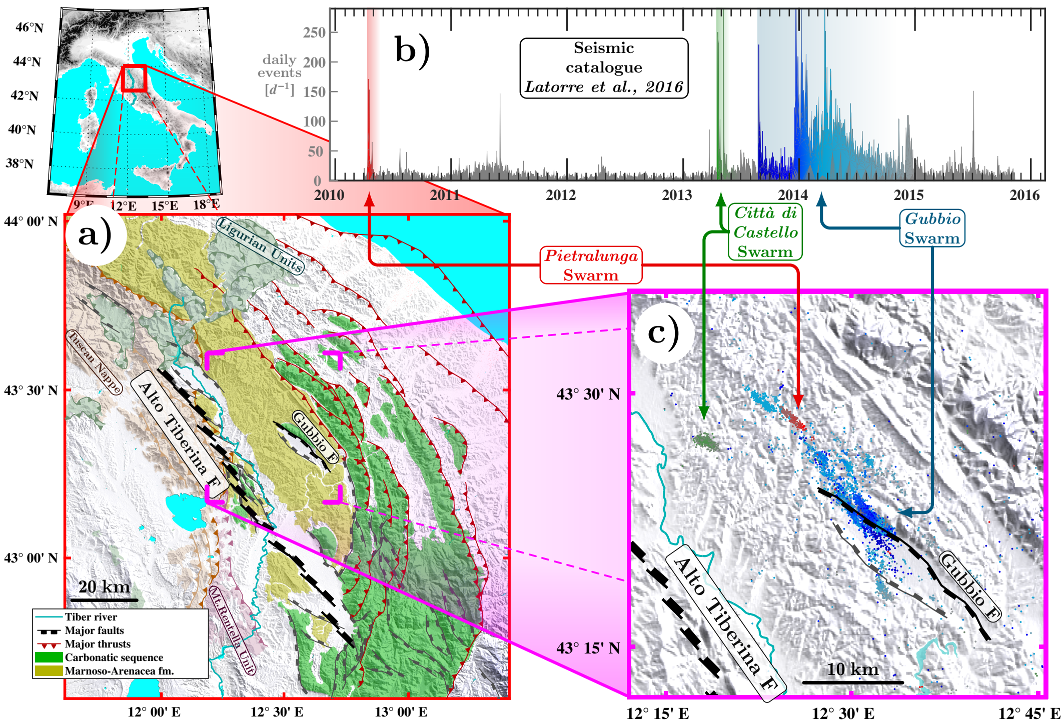

Figure 1: **a)** Location in the Italian peninsula and geological map of the ATF region, with the main tectonic units, formations, faults and thrusts. Inset showing the ATF region under study in the Italian peninsula. **b)** Temporal occurrence of the seismicity in the ATF area as the daily number of events along the 2010-2015 time period (Latorre et al., 2016): the red, green, and blue colors are used to distinguish between the *Pietralunga*, *Città di Castello* and *Gubbio* swarms, respectively. Color background highlights represent the start time and duration of each seismic swarm. **c)** Map of the epicentral locations of the local earthquake recorded during 2010-2015 (Latorre et al., 2016), in color agreement with panel b).

2 Data and Processing

In this section we describe the characteristics and processing of the different datasets included in this study: geodetic observations (GNSS), seismological recordings and meteoclimatic readings in the period between 1 January 2010 and Mid-February 2022. Every dataset acquisition network required a selection of GNSS/seismic/pluviometric stations within an area of ca. ~80 km radius set on the central section of the ATF-zone and comprising the upper Tiber basin (see Fig.2). In the case of the GNSS- and seismic- networks, the areas comprising the station selection are not limited to the upper Tiber basin, yet they sufficiently cover the watershed area.

2.1 GNSS

We use 33 GNSS stations, displayed in Fig.2a, and obtain the daily ground-displacement time series following the procedure described in Serpelloni et al. (2022). In order to increase the signal-to-noise ratio of the time series, we remove the common mode signal estimated at continental scale performing a Principal Component Analysis, as in Serpelloni et al. (2013). Furthermore, we remove the linear trend, which is estimated using the MIDAS software (Blewitt et al., 2016), from the GNSS time responses. Ultimately, we analyze the processed GNSS position time series using the Independent Component Analysis method with variational approximation and Bayesian inference (variational Bayesian ICA, Gualandi et al., 2016), which allows to separate statistically independent signals that are present in the time series. Assuming that the statistical independence of the signals means that they are caused by different processes, we associate each signal with a distinct geophysical process. In the case of this study we decompose the GNSS dataset in four Independent Components (IC's). This method has been successfully applied to extract hydrological and tectonic transient signals from geodetic displacement recordings (e.g., Gualandi et al., 2017; Serpelloni et al., 2018; Pintori et al., 2021); it uses a generative model to recreate the observations, allowing the extraction of the spatio-temporal information of an arbitrary number of independent sources of deformation from the observations, without imposing a priori any specific spatial distribution nor temporal function. The output is the definition of a limited number of sources, or IC's, characterized by a specific spatial coefficient distribution $U(\mathbf{x})$ (where $\mathbf{x}$ stands for the locations of the GNSS stations) and a time response $V(t)$. A weight coefficient is necessary to rescale their contribution in explaining the original displacement observation. In this study each IC is described by a mix of four Gaussian functions, allowing for more flexibility in the description of the sources with respect to classical ICA techniques and to consistently take into account data gaps in the displacement time series (K. Chan et al., 2003), providing also an estimate of the uncertainty associated with every IC. Hence, the displacement observations at a given station can be reconstructed by linearly summing up the contributions from all the IC's, each of which is obtained by multiplying together the specific spatial coefficient, the associated weight and the corresponding time response.

2.2 Seismic noise

We employ continuous seismic recordings from the Italian National Seismic Network (INGV Seismological Data Centre, 2006), and make a selection of 45 stations (short-period and broad-band), with a recording span longer than 6 years (see Fig.2b). For this analysis we concentrate on the seismic noise corresponding to oceanic microseisms (i.e., in the [0.1 1.0] Hz frequency range), and surface-wave signal reconstruction by cross-correlation. Our analysis involves vertical-component recordings only. Seismic processing includes standard instrumental correction, frequency band-pass filtering, spectral whitening and 1-bit normalization (Brenguier et al., 2008). Cross-correlations are carried out in 1 hour-long time sections, with half hour sliding (i.e., 50% of section overlap). In order to increase the signal reconstruction, a stacking of cross-correlation results is implemented in daily sequences. We test multiple stacking lengths to study the trade-off relation between quality in the seismic-signal reconstruction and lapse-time resolution (from 15 to 50 d). In this study we choose as most suitable the 30 d stacking-length result. We perform coda-wave interferometry (CWI, Snieder et al., 2002; Sens-Schönfelder & Wegler, 2006) on the first 26 s of seismic coda for every cross-correlation result. The analysis of the coda includes the estimate of 10 time-lag samples ($\delta\tau$) along the coda per surface-wave response. We apply a joint regression of the time lags $\delta\tau$ with respect to the coda-window time segment (τ) from all seismic-station pairs and calculate the coda-window relative time-lag variation ${}^{\delta\tau}/{}_{\tau}$. Assuming that the seismic perturbation is homogeneous throughout the study area, the final relative seismic-velocity variation (${}^{\delta v}/{}_{v}$) is given by the linear relation ${}^{\delta v}/{}_{v} = -{}^{\delta\tau}/{}_{\tau}$ (Poupinet et al., 1984; Snieder, 2006).

We produce a first set of results from the cross-correlation analysis over the complete frequency range ([0.1 1.0] Hz). A second set of results is created with exactly the same processing but applied individually over six consecutive narrower frequency bands ([0.1 0.16], [0.16 0.25], [0.25 0.36], [0.36 0.5], [0.5 0.7] and [0.7 1.0] Hz). This second set of results allows us to investigate the scattering process at different frequency ranges and thus exploit the dispersive nature of the retrieved surface waves in order to explore the depth reach of the seismic perturbations in the crust. Although small in number, the choice and amount of frequency bands analyzed is a compromise between the partitioning of the frequency range of interest, the variation of the wavefield depth sensitivity extent and the stability of the cross-correlation signal in the time domain.

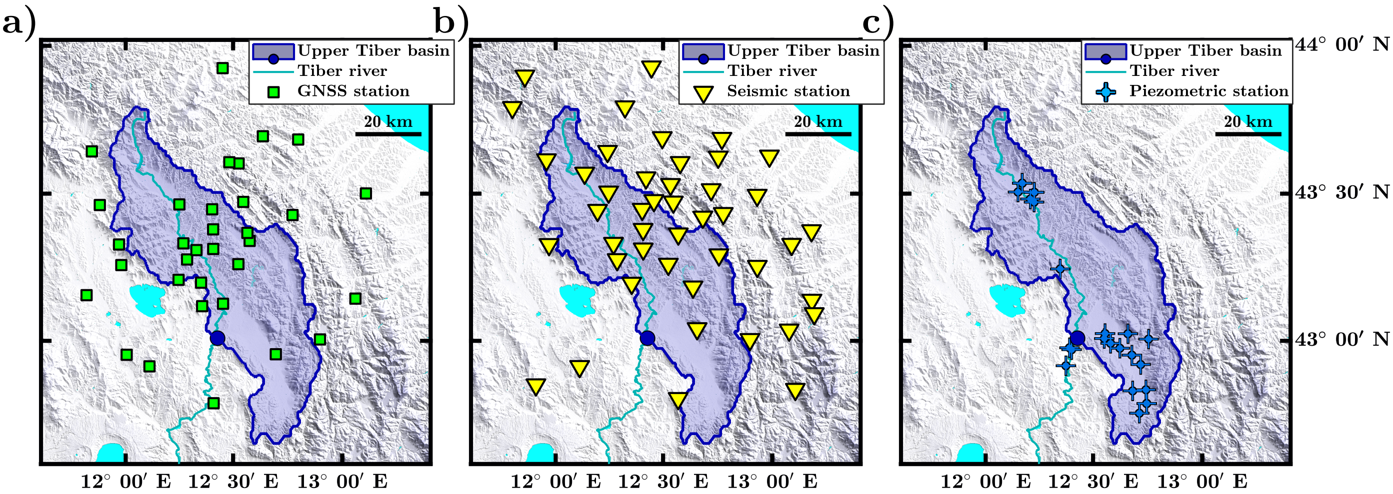

Figure 2: **a)** Location of the 33 continuous GNSS stations utilized. **b)** Distribution of the 45 permanent seismic stations of the Italian National Seismic Network selected for the seismic-noise analysis. **c)** Piezometric-sensor distribution (24) in the Umbria region used in this work. In all three panels the shadowed region depicts the upper Tiber basin taken into account for computing δTWS.

2.3 Meteo-climatic data

We take into account three kinds of meteo-climatic observations and processed data: the piezometric measurements, the hydrological balance in the upper Tiber basin in the form of total water storage variation, and the ground displacement associated with hydrological loading from a global gridded model. We calculate the Mean Piezometric Level (MPL) by performing an arithmetic mean of all the water-table readings available for this study in order to obtain an estimate representing the water-table variation in the whole upper Tiber basin. The piezometric level dataset is available at ARPA Umbria (2006) and the location of the 24 piezometric stations employed is shown in Fig.2c. In order for outlying values and single large-fluctuating piezometers not to dominate the ensemble average, we perform an amplitude normalization of every water-table reading beforehand prior to the arithmetic mean and add later an average of the respective mean values from every piezometer. We compute the total water storage variations (δTWS) in the upper Tiber basin following the method described in Pintori et al. (2021), by solving the mass balance equation between precipitation, evapotranspiration, incoming river inflow, outcoming river discharge, and potential groundwater import/export in a surrounding basin. Due to the difficulty in precisely estimating some of the parameters in the mass-balance equation, we exploit the GR5J rainfall-runoff model (Pushpalatha et al., 2011) for estimating the total water storage variations. The displacement time series associated with hydrological loading (hereinafter HL) is obtained considering the Land Surface Discharge Model (LSDM, developed by Dill, 2008). With this model approach, we estimate daily surface displacements from the continental hydrology by accounting for the precipitation, evaporation, and temperature from an atmospheric model developed by the European Centre for Medium Range Weather Forecasts (ECMWF, n.d.). We considered for this study the area with limits [11°30′E 13°E] in longitude and [43°N 44°N] in latitude.

From these three meteoclimatic products we thus obtain three independent observations related to the water content variations for the ATF zone. In Fig.4a, the δTWS and HL show a remarkable similarity and synchronized (but opposite) behaviour (-0.9 correlation coefficient). While HL is the result of a model that takes into account only the water stored in the first few meters of the subsurface, δTWS is influenced also by the groundwater. The strong similarity between HL and δTWS suggests that, in the upper Tiber basin, most of the water is stored as 'surface water' instead of groundwater, so that the groundwater-storage changes slightly influence the total water storage variations. On the other hand, the MPL time series in Fig.4b exhibits a different temporal behaviour, with more pronounced multi-annual variations (i.e., smaller maximum amplitudes for a drought period in 2012) and a persistent time delay with respect to both δTWS and HL (correlation coefficient of ∼0.7 and time lag of ∼30 d).

3 Results and Interpretation

3.1 GNSS IC decomposition

In Fig.3 we show the four IC's extracted from the GNSS-position time series. For each IC we show its corresponding time response ($V(t)$, right graph, normalized between -0.5 and 0.5) and spatial distribution ($U(\mathbf{x})$, left map). $V(t)$ describes how the displacement of the corresponding IC evolves with time, whereas $U(\mathbf{x})$ shows the maximum amplitude and 3D direction of the displacement at the location of every GNSS station $\mathbf{x}$. The color scale represents the amplitude of the maximum vertical displacement, while the yellow arrows indicate the maximum amplitude and orientation of the horizontal displacement. The displacement related to the ICn over a time interval $[t_1\ t_2]$ (with $t_2 > t_1$) at a station m is computed as $[V_n(t_2) - V_n(t_1)]\ U_n(\mathbf{x}_m)$, where $V_n(t)$ is the time response of the ICn and U_n is its corresponding spatial response.If $V_n(t)$ increases the station's horizontal displacement follows the yellow-arrow sense, while the vertical displacement is upward if the U_n vertical component is positive and downward if negative (see color scale in the maps of Fig.3).

IC1 in Fig.3 presents a clear sinusoidal behaviour with annual periodicity. The U_1 vertical components reveal a uniform response (except for one site on the NW margin). The vertical displacement of IC1's periodic signal holds a magnitude fluctuation of ca. $\sim$1 cm, while the horizontal displacement bears smaller amplitudes. Fig.4a shows the good agreement between IC1's time response and both δTWS and HL: the time series are strongly correlated (0.7 correlation coefficient) without significant time lag.

IC2 in Fig.3 shows a non-uniform spatial response both in the vertical and horizontal components. The time response of this IC exposes two different transients: the first in 2013-2014 and the second in 2016. The latter transient corresponds to the post-seismic deformation following the *Amatrice-Visso-Norcia* sequence in Central Italy, whose epicentral area is located 70-90 km south of the study area. The results are consistent, both in terms of temporal evolution and spatial response, with those presented in Mandler et al. (2021), and primarily affected the southernmost stations considered in our work. As regards the first transient signal, this is more complex to interpret. First, it shows some cross-talk with IC3. Secondly, it is of smaller entity with respect to both IC3 and the *Amatrice-Visso-Norcia* post-seismic signal. Tentatively, this small transient deformation could be associated with the *Città di Castello* seismic swarm, but the deformation pattern from the spatial response of GNSS stations in the ATF area is not that clear.

The IC3 time response also reveals a transient signal at the beginning of 2014, which is very similar both in terms of spatial distribution and temporal evolution to the one extracted by Gualandi et al. (2017). The coincidence of transient signals occurring at the end of 2013 in the time responses of both IC2 and IC3 makes it possible that cross-talk might have taken place between the two.

IC4 is described in Fig.3 as the weakest independent component in the analysis. Although its spatial coefficients show a non-uniform distribution, its time response exhibits a clear seasonal signal with a similar annual periodicity as IC1's. Fig.4b shows a good similarity of IC4's time response with the mean piezometric level at the upper Tiber basin, a solid correlation (0.7 correlation coefficient) and a ca. $\sim$30 d time lag. This suggests that the displacements associated with IC4 are related to variations of the deep portion of the water storage: we interpret the delay between the displacements and the piezometric-level variations as due to the time needed by the water to reach aquifers located deeper than the ones caught by the piezometers, whose median depth is shallower than 10 m. Furthermore, Silverii et al. (2016) and Pintori et al. (2021) interpreted a deformation pattern analogous to IC4's, characterized by anisotropic horizontal deformations with amplitudes similar to the vertical ones, caused by water-level variations in fracture systems beneath karst aquifers.

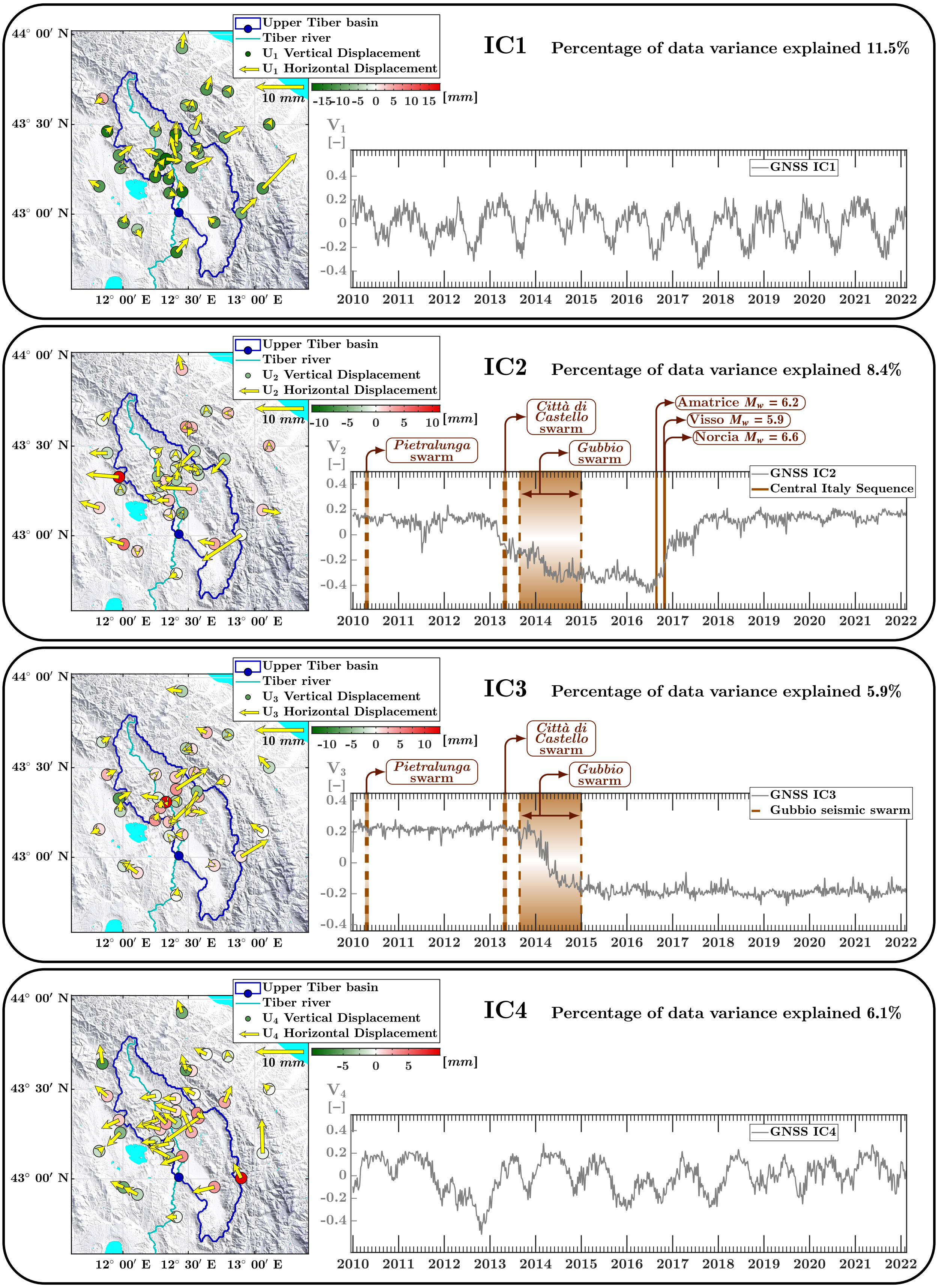

Figure 3: Time response $V_n(t)$ and spatial coefficients $U_n(\mathbf{x})$ of the four independent components: **IC1** , **IC2**, **IC3** and **IC4**. Labeled brown lines in IC2 and IC3 represent the occurrences of the three ATF seismic swarms (dashed and shadowed regions), and the three mainshocks of the Central Italy seismic sequence (solid).

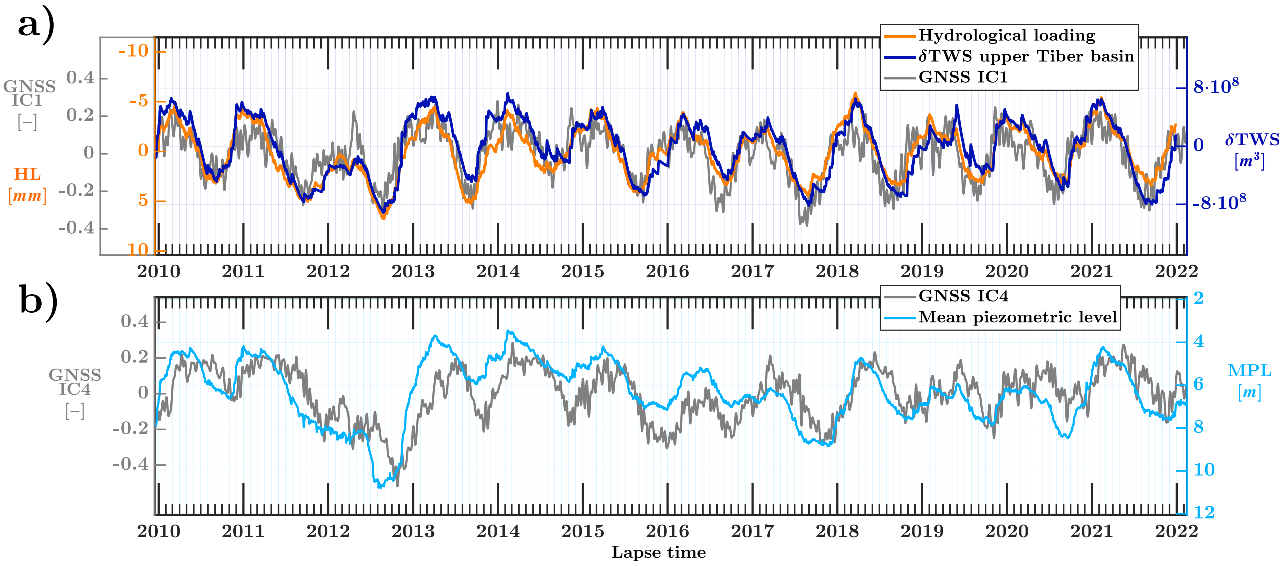

Figure 4: **a)** Time response of IC1 (namely $V_1(t)$ in Fig.3, gray) compared to the total water storage variation of the upper Tiber basin (δTWS, dark blue) and the vertical displacement caused by hydrological loading (HL, orange). Note that the HL's abscissa in the graph is reversed. **b)** Comparison between the mean piezometric level at the upper Tiber basin (MPL, light blue) and the IC4's time response (gray).

3.2 Seismic-velocity variations

In this section we present the results for the 12 year monitoring through ambient seismic noise cross-correlations. In Fig.5a we show the result of the daily-sampled relative seismic-velocity variations ($^{\delta v}/_{v}$, coloured-red line) obtained from the analysis of the data in the whole [0.1 1.0] Hz frequency band. Each daily $^{\delta v}/_{v}$ estimate is plotted at the end of the respective 30 d interval. The color scale stands for the number of $\delta\tau$ values considered in the $^{\delta\tau}/_{\tau}$ linear regression. This value represents a measure of the quality of the estimates and depends (among others) on the number of station pairs available. The color evolution, from yellow at the beginning of 2010, to red in 2012, shows how some of the employed stations have been installed during the first two years of analysis, meaning that the most stable and reliable measurements start from 2012.

For comparison, Fig.5a shows the total water storage variations of the upper Tiber basin and the IC1 temporal evolution (Fig.3a), obtained from the GNSS data analysis. The $^{\delta v}/_{v}$ result shows a remarkable anticorrelation with both the δTWS and the IC1 time series. In the 2016-2017 time period a clear divergence of the $^{\delta v}/_{v}$ result with respect to the other two time series is well observable. It corresponds to the occurrence of the 2016 Central Italy seismic sequence, which has already been attested to cause seismic-velocity variations in the crust's elastic properties at regional scale by a similar noise-based study (Soldati et al., 2019).

As for the relatively smaller local seismic swarms, the strong imprint due to the hydrological perturbation in the area buries down any significant hint of the potential tectonic perturbation of the seismic episodes in the ATF region. In an attempt to enhance the perturbation signal potentially associated with the ATF- seismic swarms, we carried out a subtraction of the hydrological perturbation using the δTWS information. Literature describes elaborate methods on how to estimate the hydrological contribution from pluviometric observations: For instance, Illien et al. (2021) uses a model with coupling soil-water and groundwater dynamics, while Rivet et al. (2015) applies poroelastic relations based on pore-pressure diffusion and homogeneous hydraulic diffusivity. In our case, given that we have an estimate of the total water content in the medium, and observe a good similarity between both the $^{\delta v}/_{v}$ and the hydrological observations, we carry out the subtraction with the aid of a scaled δTWS obtained by linear robust regression, thus avoiding any further assumptions. After applying the hydrological correction in the $^{\delta v}/_{v}$ result the strong seasonal behaviour vanishes whereas the identification of perturbations related to the ATF-swarms remains not visible at all (see Fig.5b).

The second set of results, obtained from multiple consecutive narrow- frequency bands, allowed us to explore the perturbation response in the medium at the study site in multiple depth-sampling ranges (Hobiger et al., 2012). Fig.6 shows the corresponding $^{\delta v}/_{v}$ results from each of the six frequency bands analyzed, with respect to the time response of IC1 and the δTWS result. In these results we observe that the seasonal behaviour of the seismic-velocity perturbations decreases as we lower the frequency-content, but always remains present nonetheless. The resemblance between the δTWS and the $^{\delta v}/_{v}$ results with the higher frequency content (Figs.6a, 6b and 6c) is indicated in their corresponding Pearson's correlation coefficients: -0.71, -0.82 and -0.69, respectively. This is expected since the crustal depth-sampling range gets shallower, and thus more exposed to effects from perturbations due to surface/hydrological phenomena. Also, the top frequency-band results bear a foreseeable time delay (~15 d as estimated by cross-correlating the two time series) with respect to the δTWS, produced by the cross-correlation 30-day stacking bias. However, in the lowest frequency-band $^{\delta v}/_{v}$ results (Fig.6e and 6f) their low correlation coefficient (-0.47 and -0.44, respectively) show a weaker effect of the yearly seasonality, hence revealing the diminishing effect of hydrological perturbations as we sample deeper the scattering wavefield in the crust.

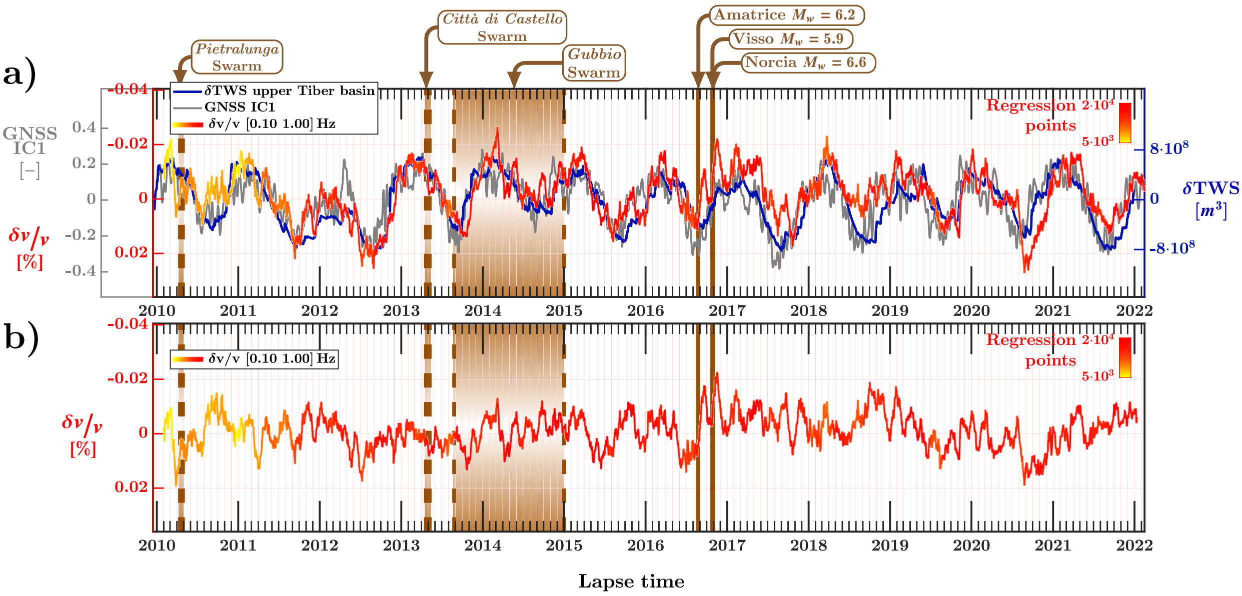

Figure 5: Comparison of geodetic (GNSS IC1) and hydrological (δTWS) observations with the relative seismic-velocity variations ($^{\delta v}/_{v}$), the latter displayed with reversed abscissa. Brown lines depict the bounds of the occurrence periods of the ATF seismic swarms (dashed) and the mainshock occurrences of the seismic sequence of Central Italy (solid). **a)** $^{\delta v}/_{v}$ result obtained from the complete frequency band [0.1 1.0] Hz, compared to the δTWS and the IC1 time response. **b)** Same $^{\delta v}/_{v}$ result in a) after applying a hydrological correction based on the δTWS result.

This detail indicates that seismic-velocity perturbations at depths larger than 3 km seem to be driven by phenomena other than surface hydrology.

In order to constrain the depth range of the results in Fig.6, we create a series of 1-D models that account for the depth characteristics of the mechanical properties of the study site. From the catalogue of oil-exploration activities carried out in the area (Progetto ViDEPI, 2009-2023) we select the boreholes with best logging completeness and largest depth reach (>2.5 km), and build five different 1-D geological models. We utilize the logging data to describe the elastic properties in depth and complete the missing information with values obtained from literature (Ciccotti et al., 2004; Trippetta et al., 2010; Ji et al., 2018; Chicco et al., 2019; Montone & Mariucci, 2020). We use the 1-D elastic models to calculate the fundamental-mode depth-sensitivity kernels of Rayleigh-wave phase velocity in order to observe the depth range where each of the frequency-band results is dominant (Herrmann, 2013). The depth-sensitivity kernels from the corresponding frequency bands of analysis are shown in Fig.7a for each of the locations, with the 1-D geological model of the corresponding borehole displayed in the background. Both $^{\delta v}/_{v}$ results in Fig.6 and depth-sensitivity curves in Fig.7a share the same color code by frequency band.Only depth-sensitivity kernels with respect to shear-wave velocity (β) perturbations are shown. Fig.7b depicts the dispersion curve of the Rayleigh-wave fundamental mode in the *Monte Civitello* 1-D model (based on the "Monte Civitello 001" borehole, Fig.7a) with respect to the six frequency bands of analysis, while Fig.7c shows the map distribution of the selected boreholes.

The use of multiple models serve to account for the varying depth sensitivity given the extension and geological complexity of this sector of the Apennines (see Figs.1a and

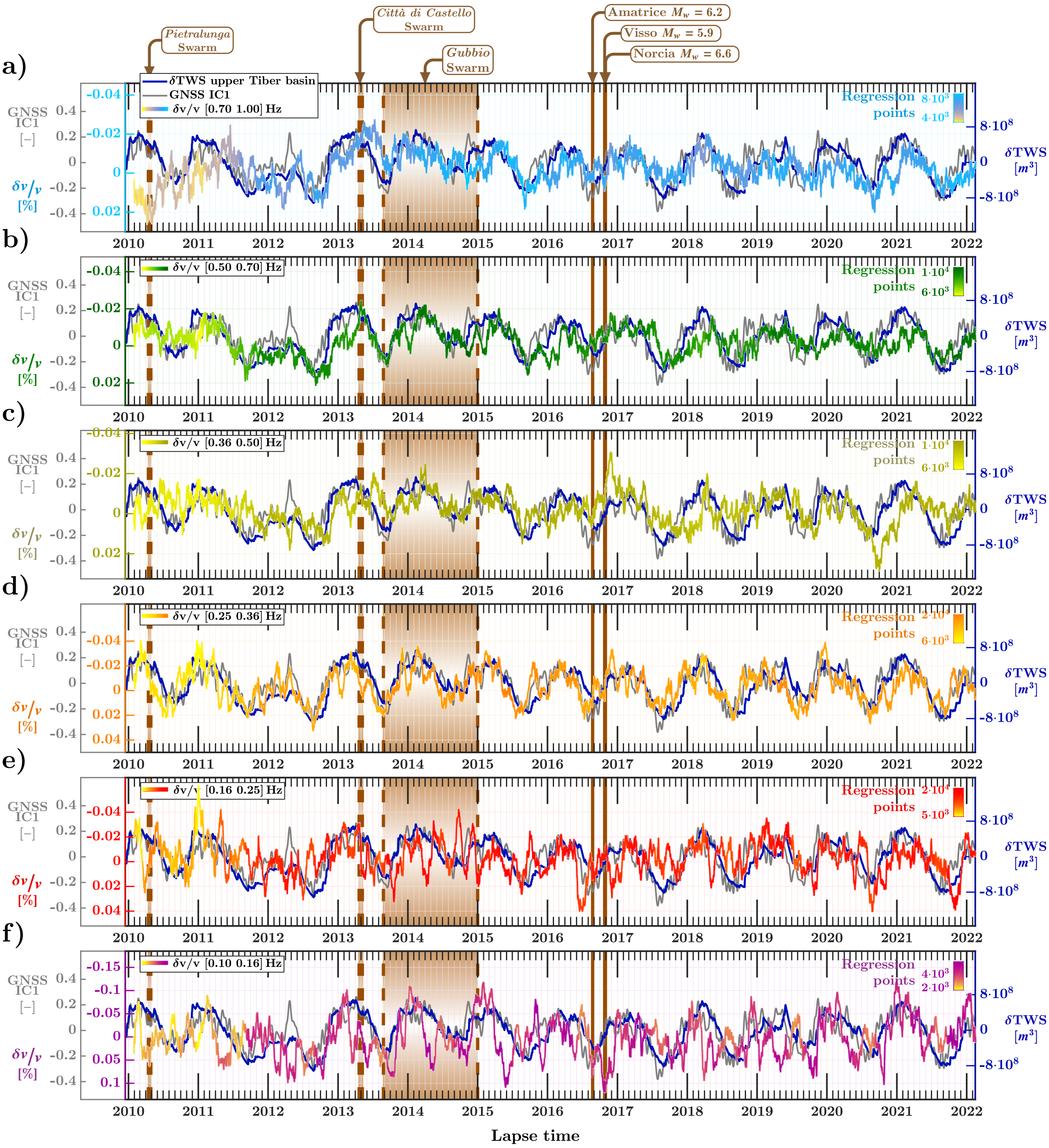

Figure 6: Comparison of GNSS IC1 time response, δTWS and ${}^{\delta v}/_{v}$ (abscissa-reversed) for different frequency bands: **a)** [0.7 1.0] Hz. **b)** [0.5 0.7] Hz. **c)** [0.35 0.5] Hz. **d)** [0.24 0.35] Hz. **e)** [0.16 0.24] Hz. **f)** [0.1 0.16] Hz. Brown lines represent the bounds of the occurrence periods of the ATF seismic swarms (dashed lines and shadowed region) and the mainshock occurrences of the seismic sequence of Central Italy (solid).

Fig.7c). Following this, the "San Donato 001" borehole represents the depth sensitivity of Rayleigh waves in the western area of the study site, in a model with shallow siliciclastic sequences and thick levels of the Burano formation. To the North, the

"Pieve S.Stefano 001" borehole provides a model with larger siliciclastic sequences and repeated carbonatic sequences in depth. The "Burano 001" and "Fossombrone 002" boreholes depict the thrust-and-fold complexity in the East and South of the study site: their corresponding graphs describe the Rayleigh-wave sensitivity when the medium is characterized by massive (duplexed-) carbonatic sequences of larger extension in depth. The borehole "Monte Civitello 001" provides a model of the central section of the study site, with a thick display of the Umbro-Marchigian formation and the complete carbonatic series in a single sequence.

For our final monitoring analysis, we make use of the elastic 1-D models and integrate all our multiple frequency-band results in order to estimate a depth distribution of the elastic-properties' perturbation that can describe the observed relative seismic-velocity variations at their respective frequency-band ranges. We implement the methodology for inversion of surface-wave dispersion curves (Dorman & Ewing, 1962; Szelwis & Behle, 1984; Socco & Strobbia, 2004) and adapt it to produce a depth-image result of the crustal perturbations observed in our $\delta v/v$ results at every lapse time. The description of the elastic properties in the 1-D models in Fig.7a enables the estimation of the (fundamental-mode) phase-velocity function for a laterally homogeneous medium with respect to the frequency values described within the depth limits of the model (see Fig.7b). Associating the multiple frequency-dependent $\delta v/v$ with the phase-velocity function we can constrain the physical magnitude of the phase-velocity perturbation δv for every frequency band at every lapse time. With the magnitude estimate of the phase-velocity change, we employ the depth-sensitivity kernels in Fig.7a to calculate the perturbation of the elastic properties of the medium. Since shear-wave velocity dominates propagation properties of Rayleigh waves (Xia et al., 1999; Louie, 2001; Wathelet et al., 2004), and assuming no mass-density changes happen in the medium, in this analysis we assume the crustal perturbations to be caused by shear-modulus changes ($\delta\mu$). In our approach, although the medium is simplified by assuming a stratified 1-D inhomogeneous half space, we disregard the retrieval of Rayleigh-wave higher-mode waveforms in our cross-correlation scattering coda given the geological complexity of the subsurface across the area and the strong variability of the geological structure (see Fig.7a) for the frequency range of our study. Hence, we neglect in our analysis any effect caused by the presence of cross-mode cross-correlation artefacts in our scattering coda (Kimman & Trampert, 2010). In our analysis the scattering is assumed to be controlled exclusively by the Rayleigh-wave fundamental mode and hence we neglect any Rayleigh-to-Rayleigh and Love-to-Rayleigh scattering mode conversions in the retrieved cross-correlation coda (Snieder, 1986). The depth-sensitivity kernels employed are originally conceived for Rayleigh-wave direct-arrival analysis and do not account for surface- to body-wave mode conversions (Chang & Tuan, 1973; Tuan, 1975; Momoi, 1981). Yet, Rayleigh-to-Rayleigh scattering mode becomes dominant with time because of their weaker decay (Maeda et al., 2008). Since our analysis mostly comprises late coda arrivals, and due to the fact that Rayleigh-to-Rayleigh scattering mode has a weaker decay (t^{-1}) with respect to the Rayleigh-to-body wave mode (t^{-4}), we neglect any scattering body-wave conversion and run under the premise that the analyzed coda is dominated by scattered Rayleigh waves.

For the inversion process we apply regularized damped least-squares (Tarantola & Valette, 1982; Haney & Tsai, 2017), employing the error estimate at each $\delta v/v$ regression result in order to build the diagonal data-covariance matrix. Although we counted on six frequency-band results, given the ill-posedness of our problem we employ 20 frequency samples, implying a repetitive use of the $\delta v/v$ time series but with varying amplitude, following the corresponding 1D model phase-velocity curve (see Fig.7b).

The final result we produce is a depth-monitoring image: a time-lapse with the depth distribution of crustal perturbations detected by our seismic stations assuming a laterally invariant medium, with isotropic scattering properties, and thus neglecting lateral

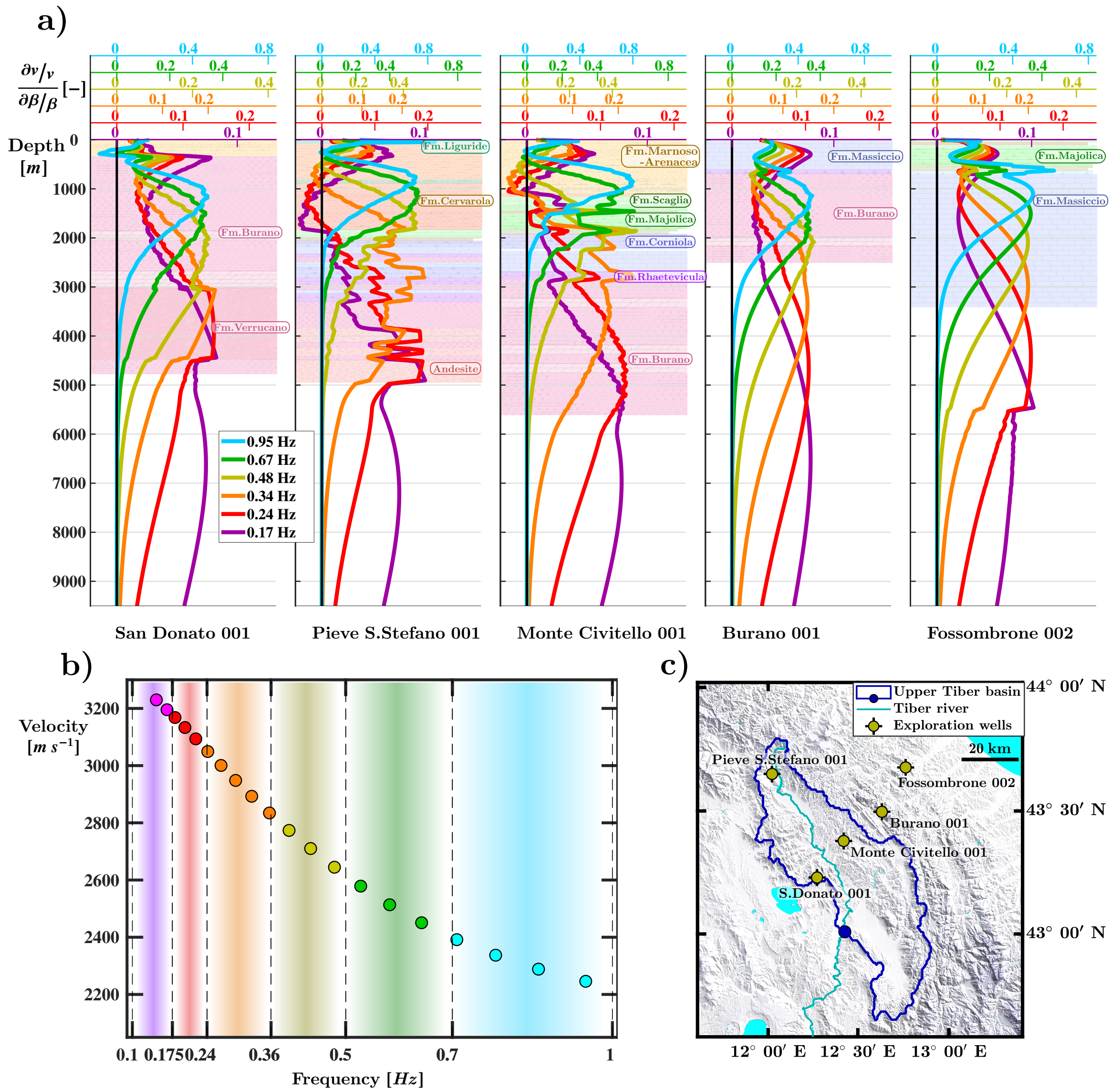

Figure 7: Depth sensitivity analysis: **a)** Fundamental-mode Rayleigh-wave depth-sensitivity kernels from five different 1-D geological models. Top colored axes define the amplitude values of their corresponding color-matching kernel. Main geological formations are named with colored labels. The geological models are based on the logging results of the respective boreholes, named at the bottom of their respective figure. The depth-sensitivity kernels correspond to phase-velocity sensitivity with respect to a perturbation in the shear-wave velocity (β), at the six frequency bands analyzed (see matching-color correspondence with results in Fig.6). **b)** Phase-velocity samples employed for the depth-monitoring imaging. Phase velocity values of the fundamental-mode Rayleigh wave for the *Monte Civitello* 1-D model in a). The colour of each frequency sample indicates to which of the 6 analyzed frequency bands it corresponds, and in turn which $\delta v/v$ time series in Fig.6 is employed during the depth-monitoring imaging process. **c)** Location of the boreholes from which the 1-D elastic models in a) were built.

perturbation-distributions. This sort of monitoring result has recently been presented in Fokker et al. (2023), where they adapt their depth-sensitivity kernels to retrieve the depth distribution of hydrologically-induced seismic perturbations in the form of pore-pressure variations.

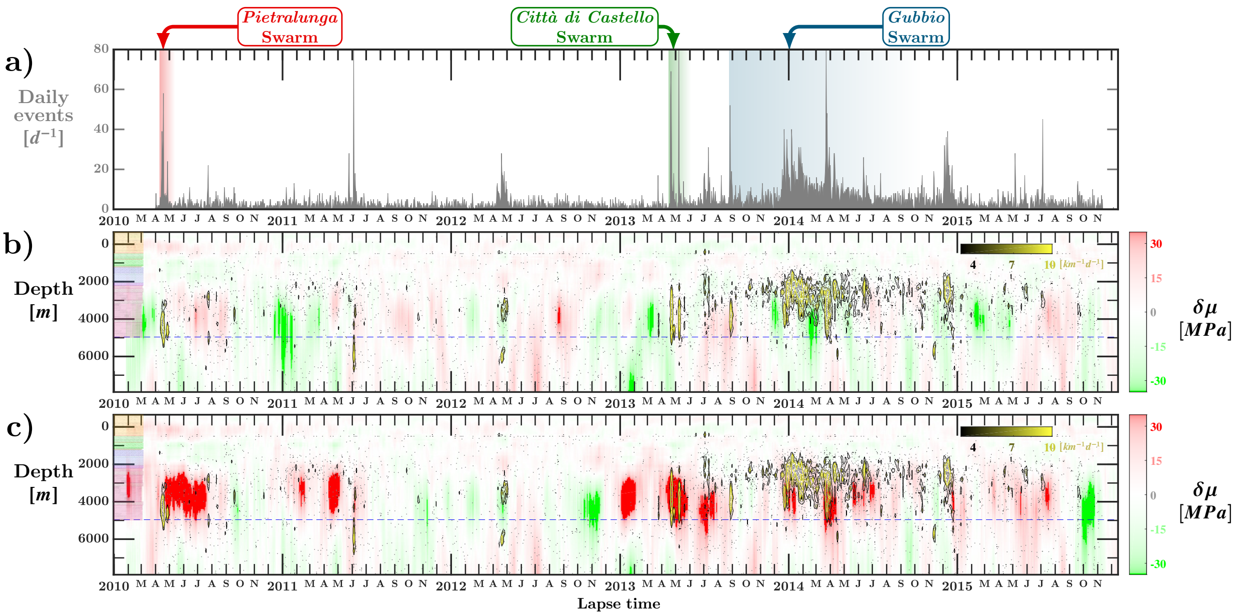

Figure 8: Depth-imaging monitoring of shear-modulus changes ($\delta\mu$) compared with the depth distribution of the seismic events in the ATF zone. Depth model is based on the "Monte Civitello 001" borehole (see Fig.7a). **a)** Daily number of seismic events with magnitude greater than the completeness magnitude ($M_L > 0.5$) in the ATF zone, as in the catalogue shown in Fig.1b. **b)** Monitoring of the crustal shear-modulus perturbation in depth from the multiple frequency-band $^{\delta v}/_{v}$ results. Seismic events in a) are displayed as individual dots and as a contour-density map in time and depth (color magnitudes in events per day and kilometer). Dashed blue line represents the limit of the "Monte Civitello 001" borehole. **c)** Same as in b), after applying the correction of the hydrologically induced perturbations with the aid of the Total Water Storage variation (δTWS) estimate.

Fig.8a shows the daily occurrence of seismic events from the seismic catalogue depicted in Fig.1b with magnitude greater than the completeness magnitude ($M_L > 0.5$, Pastoressa et al., 2023). The depth-imaging monitoring results displayed in Fig.8b and Fig.8c correspond to the use of the *Monte Civitello* 1-D model. Results are displayed in depth using the mean sea level as permanent datum and the measured depth has been shifted with respect to the "Monte Civitello 001" drill floor. The dashed blue line depicts the limit of the borehole in depth, which means that the model becomes homogeneous beyond this limit. The depth versus time of the complete catalogue (i.e., only seismic events with $M_L > 0.5$) is superimposed.

Without applying any hydrological correction, the depth-imaging monitoring shows that the shear-modulus perturbations happen independently from the time occurrence of seismic events (Fig.8b). On the other hand, Fig.8c shows the result of applying the same inversion technique on the multiple frequency-dependent relative seismic-velocity variation results after applying an individually-customized δTWS-based correction of the hydrological seismic perturbation on each $^{\delta v}/_{v}$ time series (sane correction applied in the $^{\delta v}/_{v}$ result of Fig.5b). In these results one can easily identify blunt increases in the medium's shear modulus at the occurrence time of seismic swarms, in the range of tens of MPa and always within the seismogenic depth range (roughly between 2 and 5 km of depth). At the same time of the *Pietralunga* swarm, an increase of $\delta\mu$ sustained in time for 3 months is observed; high density seismic occurrences in the first half of 2011 coincide with short duration crustal shear-modulus perturbations. The second half of 2011 and the whole 2012 show a time interval of small perturbations concurring with a period of seismic quiescence. Then, an increase of crustal shear-modulus perturbation occurs in January 2013 (no seismic activity has been recorded at this time), and in April-May 2013 with the *Città di Castello* swarm occurrence. During the *Gubbio* seismic swarm $\delta\mu$ shows a first perturbation coinciding with the maximum magnitude event in December, 2013, followed by a larger and longer perturbation corresponding to the second peak of events in March-April, 2014. Later perturbation episodes during 2014 and 2015 match with seismic occurrences of smaller time concentration.

4 Discussion

We use the δTWS, the displacement associated with hydrological loading (HL) and the mean piezometric level (MPL) for the period 2010-2022 in order to get three independent observations related to temporal variations in water content of the shallow crust. The MPL, although showing a similar trend with the HL and the δTWS, displays a 30 d delay with respect to the latter two, but a good agreement and reduced time lag with IC4 from GNSS decomposition. These last two time series may be representative of possible local effects related with the southernmost region of the upper Tiber basin where most of the piezometric wells are located (Fig.2c) and also the GNSS stations show the maximum (vertical) displacements associated with IC4 (Fig.3).

Total water content variations are known to cause measurable ground deformations (from GNSS data analysis) but also affect the elastic parameters of the superficial crustal sections (from noise-based monitoring analysis). In the ATF area, if from one side the hydrological perturbations seem to be responsible for two independent components out of the four produced by the variational Bayesian ICA decomposition of GNSS time responses, its influence on perturbation of elastic parameters is still visible up to the first few km of depth (in the $^{\delta v}/_{v}$ results at frequency ranges from 0.25 to 1 Hz). Regarding the first point, this means that the TWS variations are the most important source of seasonal modulation of crustal deformation (~18% of data variance explained compared to the 14% of the seismic activity components as from Fig.3). Similarly, a relevant influence of δTWS arises from the $^{\delta v}/_{v}$ temporal variations of Fig.5 where the two time series show a very good anticorrelation (correlation coefficient of -0.81) and limited time lag (ca. ~4 d). Interestingly, this relationship holds also for most of the six shorter frequency bands (Fig.6). In particular we can observe a good anticorrelation (correlation coefficient < -0.5) for the higher frequency bands down to the fourth one [0.25 0.35] Hz. While for the two lower frequency bands (i.e., [0.1 0.17] and [0.17 0.25] Hz), i.e., the deepest portions of the crustal volume investigated, the periodic behavior associated with the δTWS is not visible anymore. By looking at the depth-sensitivity kernels of Fig. 7a we observe that these last two frequency range waves (red and magenta lines) are sampling deeper levels of the Earth's crust (roughly from 4 km depth further down for all crustal-structure models from all borehole locations), compared to the higher frequencies that are sensitive to the first 2-4 km of depth from the surface. Therefore we observe an influence of the TWS variations on the relative seismic-velocity variations in the crust until a depth of few km as already found also in other areas (Poli et al., 2020; Barajas et al., 2021; Almagro Vidal et al., 2021), thus indicating this observation as a possible general feature from the Southern and Central Apennines to the Alpine regions. Beside the δTWS influence, we could also observe that the co- and post-seismic variations associated with the 2016 Central Italy seismic sequence are mainly visible only in the two middle frequency ranges ([0.25 0.35] and [0.35 0.5] Hz), roughly corresponding to a depth range of 2-4 km. This may be explained by the presence of a CO_2 highly pressurized crustal level (Chiodini et al., 2004; Carannante et al., 2013), which may be able to amplify the effect of the shaking (as similarly seen also in Brenguier et al., 2014).

The strong influence of water content variations is easily separated from other sources of crustal perturbation in the GNSS data by applying variational Bayesian IC analysis (see Fig.3). For the relative seismic-velocity variations instead, the removal of the δTWS influence does not provide clear information on other possible sources of seismic perturbations, at least none clearly related to seismic swarm occurrences (Fig.5b). In order to improve exposure of the perturbations, we apply an inversion approach integrating the six frequency-band $^{\delta v}/_{v}$ results with the aid of their depth sensitivity and local 1-D elastic models of the crustal structure in depth. This procedure provides the monitoring of the crustal perturbations expressed in the form of shear-modulus variations and depicted as a depth distribution (Fig.8). In this case the removal of the hydrologically-induced seismic perturbation is carried out before inversion for each of the six $\delta v/v$ time series individually, with an independent scaling based on the similarity of each frequency-band $\delta v/v$ result with the δTWS. The final result unveils crustal shear-modulus perturbations displaying some conformity with the occurrence time and seismogenic depth of the ATF seismic swarms (Fig.8c). Our results describe an increase of crustal $\delta\mu$ concurrent with the seismic swarms, which is interpreted as the result of an increase in the compliance of the rock's pore space following a decrease in pore pressure (Freund, 1992; Khaksar et al., 2001; Shapiro, 2003). This is contrary to the main earthquake-generator process considered by the vast majority of research work in the region: the increase in pore pressure leading to a decrease of the effective stress on the fault plane, thus favoring the rupture (Rice, 1992; Axen, 1992; Miller et al., 1996). In agreement with this interpretation, a recent study also based on $\delta v/v$ analysis depicts a seismic-velocity decrease during the activity period of the *Città di Castello* and *Gubbio* swarms (Mikhael et al., 2024). Although they account for the perturbation effect produced by meteoclimatic phenomena in their analysis, the use of auto-correlation instead of cross-correlation, and the different frequency range and stacking-length employed makes the result comparison unsuitable.

The presence of overpressurized fluids in the upper crustal section (from few to 15 km of depth) under the Apennine belt has been extensively referred to as a primary source of instability and possibly the major triggering mechanism for the seismicity of this area (Chiodini et al., 2004), especially for the 1997-1998 Umbria-Marche seismic sequence (Quattrocchi, 1999; Chiarabba et al., 2009; Miller et al., 2004). Fluid circulation within the fault zone favours the replacement of strong minerals in the fault gouge which lead to frictional instabilities or fault weakening (Collettini et al., 2019; Volpe et al., 2022). This is expected at large depths, that explain the presence of the Alto Tiberina fault (Chiaraluce et al., 2007; Hreinsdóttir & Bennett, 2009; Vadacca et al., 2016), yet our observations refer to the normal-fault splay distributed in the ATF's hanging wall, at shallower levels. The sign of the crustal perturbations observed in our noise-based monitoring and its correlation with the seismic-swarm occurrences, however, reveal that the earthquake nucleation process might require further discussion, and could shed light on an alternative physical interpretation. Local seismic tomography imaging has revealed high pore-pressure conditions in depth (from 3 km, Piana Agostinetti et al., 2017; Chiarabba et al., 2020), which are confirmed by in situ readings of CO_2 pressure in deep exploration boreholes ("Pieve S.Stefano 001", "San Donato 001"). The observed increase in shear modulus in our results shows the fault rupture to be apparently driven by the poroelastic stress path defined by the pore-pressure relaxation following crustal CO_2 degassing. Some studies have referred to the fluid migration originating from mainshocks and their corresponding pore-pressure relaxation as the trigger to aftershock seismicity (Miller et al., 2004; Antonioli et al., 2005). Dahm & Fischer (2014) monitor changes on the V_P/V_s ratio on three mid-crustal swarms in NW-Bohemia over a 10 year span and identify abrupt decreases of the body-wave velocity ratio at the source region before and during the main seismic activity. They explained this observation as due to the degassing process of overpressurized fluids during the beginning phase of the swarm activity. Although we observe our perturbations in the form of shear-modulus increases, the former observation becomes similar to our $\delta\mu$ increase considering that the sensitivity kernels used in the inversion are based on shear-wave velocity changes. Moreover, within the Central Italy sequence, Chiarabba et al. (2020b) distinguished a precursory increase in body-wave velocity prior to the Norcia mainshock followed by an abrupt decrease at the time of rupture. Pore-pressure relaxation induces changes in the horizontal stress field, increases effective stress (A. Chan & Zoback, 2002; Zoback & Zinke, 2002) and defines stress paths that induce reactivation faulting (Hillis, 2000; Hettema, 2020; Van den Bogert & van Eijs, 2020). In future works we intend to confirm the increase in the crustal shear modulus associated with CO_2-degassing episodes by comparing our new results with recently available continuous CO_2-flux measurements in the field.

5 Conclusions

We have successfully integrated seismological, geodetic and hydrological observations in a multidisciplinary framework to monitor the deformation and changes in mechanical properties of the crust in the ATF zone. Our study identifies and quantifies the perturbation effect in the crust produced by surface phenomena and seismic activity, confirming the strong effect that surface hydrology plays in the monitoring results. The analysis of GNSS position time series with blind source separation highlights seasonal deformation signals associated with changes in water storage and surface hydrology and transient deformation signals associated with tectonic events.

We find that hydrologically-induced seismic perturbations are dominant in the $^{\delta v}/_{v}$ results from ambient seismic noise, masking weaker signals associated with minor tectonic events, such as low energy seismic swarms. If from one side, ambient seismic noise recordings successfully enable the continuous monitoring of the hydrological changes, estimates of the total water storage variation can be used as a proxy for the hydrologically-induced seismic perturbations in order to quantify its impact and hence apply its correction. Yet, even with this hydrological-effect correction the seismic perturbations related to the ATF seismic swarms remain unclear. The analysis of the $^{\delta v}/_{v}$ in reduced frequency bands can serve as an approach for detecting small-to-moderate-amplitude perturbations associated with low energy seismic swarms. By varying the frequency content, we analyze the seismic perturbations in consecutive overlapping depth ranges and get a better depth inspection of the crustal elastic-properties' variations caused by the local seismic swarms. The use of 1-D models based on well logging surveys can provide valuable information in the estimation of the penetration range of the seismic perturbations. Moreover, the estimation of the phase velocities based on the 1-D models facilitates an estimation of the magnitude of the seismic-velocity perturbation per frequency range. This estimate enables us to apply a perturbational inversion of the crustal changes, presented in the form of shear-modulus variations, and retrieve its distribution in depth at every lapse time. With the necessary correction for the hydrological-effect by means of the δTWS, this 1-D depth-monitoring imaging approach highlights seismic perturbations of the crustal properties that concur with the time of occurrence and depth range of the ATF seismic swarms. Our final results instill doubts on the manifold role of fluid migrations in the seismic swarms' generation processes in the Alto Tiberina Fault zone.

Data availability statement

Geodetic data provided by *Istituto Nazionale di Geofisica e Vulcanologia* (Serpelloni & Pintori, 2024), accessible at https://zenodo.org/records/10809324. Groundwater level data provided by (ARPA Umbria, 2006), available at https://apps.arpa.umbria.it/acqua/contenuto/Livelli-Di-Falda. Hydrological load model from (Dill & Dobslaw, 2013), dataset accessible at http://rz-vm115.gfz-potsdam.de:8080/repository/entry/show?entryid=24aacdfe-f9b0-43b7-b4c4-bdbe51b6671b. The precipitation, temperature, and river-flow data used to implement the hydrological model provided by (Servizio Idrografico Regione Umbria, 2021–2024), and available at https://annali.regione.umbria.it/, https://www.sir.toscana.it/consistenza-rete, https://console.regione.marche.it/(http://app.protezionecivile.marche.it/sol/indexjs.sol?lang=it), for the regions of Umbria, Tuscany, and Marche, respectively. Extraterrestrial irradiance data accessible at http://www.soda-pro.com/web-services/radiation/extraterrestrial-irradiance-and-toa. Drainage direction maps used to define river basins available at www.hydrosheds.org/page/availability. Seismic data provided by *Istituto Nazionale di Geofisica e Vulcanologia* (INGV Seismological Data Centre, 2006), accessible at https://eida.ingv.it/it/.Well logs utilized to build the 1-D elastic models accessible at (Progetto ViDEPI, 2009-2023).

References

Almagro Vidal, C., Zaccarelli, L., Pintori, F., Bragato, P. L., & Serpelloni, E. (2021). Hydrological effects on seismic-noise monitoring in karstic media. *Geophysical Research Letters*, *48*(15), e2021GL093191. doi: 10.1029/2021GL093191

Andajani, R. D., Tsuji, T., Snieder, R., & Ikeda, T. (2020). Spatial and temporal influence of rainfall on crustal pore pressure based on seismic velocity monitoring. *Earth, Planets and Space*, *72*(1), 1–17. doi: 10.1186/s40623-020-01311-1

Anderlini, L., Serpelloni, E., & Belardinelli, M. E. (2016). Creep and locking of a low-angle normal fault: Insights from the Altotiberina fault in the Northern Apennines (Italy). *Geophysical Research Letters*, *43*(9), 4321–4329. doi: 10.1002/2016GL068604

Anggono, T., Nishimura, T., Sato, H., Ueda, H., & Ukawa, M. (2012). Spatio-temporal changes in seismic velocity associated with the 2000 activity of Miyakejima volcano as inferred from cross-correlation analyses of ambient noise. *Journal of volcanology and geothermal research*, *247*, 93–107. doi: 10.1016/j.jvolgeores.2012.08.001

Antonioli, A., Piccinini, D., Chiaraluce, L., & Cocco, M. (2005). Fluid flow and seismicity pattern: Evidence from the 1997 Umbria-Marche (central Italy) seismic sequence. *Geophysical Research Letters*, *32*(10). doi: 10.1029/2004GL022256

ARPA Umbria. (2006). *Agenzia Regionale per la Protezione Ambientale Umbria.* Sistema Nazionale per la Protezione dell'Ambiente. Retrieved from https://apps.arpa.umbria.it/acqua/contenuto/Livelli-Di-Falda (Last accessed: March 12, 2024)

Axen, G. J. (1992). Pore pressure, stress increase, and fault weakening in low-angle normal faulting. *Journal of Geophysical Research: Solid Earth*, *97*(B6), 8979–8991. doi: 10.1029/92JB00517

Barajas, A., Poli, P., d'Agostino, N., Margerin, L., & Campillo, M. (2021). Separation of poroelastic and elastic processes of an aquifer from tectonic phenomena using geodetic, seismic, and meteorological data in the Pollino region, Italy. *Geochemistry, Geophysics, Geosystems*, *22*(11), e2021GC009742. doi: 10.1029/2021GC009742

Bettinelli, P., Avouac, J.-P., Flouzat, M., Bollinger, L., Ramillien, G., Rajaure, S., & Sapkota, S. (2008). Seasonal variations of seismicity and geodetic strain in the Himalaya induced by surface hydrology. *Earth and Planetary Science Letters*, *266*(3-4), 332–344. doi: 10.1016/j.epsl.2007.11.021

Blewitt, G., Kreemer, C., Hammond, W. C., & Gazeaux, J. (2016). MIDAS robust trend estimator for accurate GPS station velocities without step detection. *Journal of Geophysical Research: Solid Earth*, *121*(3), 2054–2068. doi: 10.1002/2015JB012552

Brenguier, F., Campillo, M., Hadziioannou, C., Shapiro, N., Nadeau, R., & Larose, E. (2008). Postseismic relaxation along the San Andreas Fault at Parkfield from continuous seismological observations. *Science*, *321*(5895), 1478–1481. doi: 10.1126/science.1160943

Brenguier, F., Campillo, M., Takeda, T., Aoki, Y., Shapiro, N., Briand, X., ... Miyake, H. (2014). Mapping pressurized volcanic fluids from induced crustal seismic velocity drops. *Science*, *345*(6192), 80–82. doi: 10.1126/science.1254073

Brenguier, F., Shapiro, N., Campillo, M., Ferrazzini, V., Duputel, Z., Coutant, O., & Nercessian, A. (2008). Towards forecasting volcanic eruptions using seismic noise. *Nature Geoscience*, *1*(2), 126–130. doi: 10.1038/ngeo104

Budi-Santoso, A., & Lesage, P. (2016). Velocity variations associated with the large 2010 eruption of Merapi volcano, Java, retrieved from seismic multiplets and ambient noise cross-correlation. *Geophysical Journal International*, *206*(1), 221–240. doi: 10.1093/gji/ggw145

Campillo, M. (2006). Phase and correlation in 'random' seismic fields and the reconstruction of the Green function. *Pure and applied geophysics*, *163*, 475–502. doi: 10.1007/s00024-005-0032-8

Carannante, S., Monachesi, G., Cattaneo, M., Amato, A., & Chiarabba, C. (2013). Deep structure and tectonics of the Northern-Central Apennines as seen by regional-scale tomography and 3-D located earthquakes. *Journal of Geophysical Research: Solid Earth*, *118*(10), 5391–5403. doi: 10.1002/jgrb.50371

Chan, A., & Zoback, M. (2002). Deformation analysis in reservoir space (DARS): a simple formalism for prediction of reservoir deformation with depletion. In *SPE/ISRM Rock Mechanics Conference.* Society of Petroleum Engineers. doi: 10.2118/78174-MS

Chan, K., Lee, T.-W., & Sejnowski, T. J. (2003). Variational Bayesian learning of ICA with missing data. *Neural Computation*, *15*(8), 1991–2011. doi: 10.1162/08997660360675116

Chang, C., & Tuan, H. (1973). On the surface-to-bulk mode conversion of Rayleigh waves. *IEEE Transactions on Microwave Theory and Techniques*, *21*, 558–560. doi: 10.1109/TMTT.1973.1128060

Chiarabba, C., Buttinelli, M., Cattaneo, M., & De Gori, P. (2020). Large earthquakes driven by fluid overpressure: The Apennines normal faulting system case. *Tectonics*, *39*(4), e2019TC006014. doi: 10.1029/2019TC006014

Chiarabba, C., De Gori, P., & Boschi, E. (2009). Pore-pressure migration along a normal-fault system resolved by time-repeated seismic tomography. *Geology*, *37*(1), 67–70. doi: 10.1130/G25220A.1

Chiarabba, C., De Gori, P., Segou, M., & Cattaneo, M. (2020b). Seismic velocity precursors to the 2016 Mw 6.5 Norcia (Italy) earthquake. *Geology*, *48*(9), 924–928. doi: 10.1130/G47048.1

Chiaraluce, L., Amato, A., Carannante, S., Castelli, V., Cattaneo, M., Cocco, M., ... others (2014). The Alto Tiberina Near Fault Observatory (Northern Apennines, Italy). *Annals of Geophysics*, *57*(3), S0327. doi: 10.4401/ag-6426

Chiaraluce, L., Chiarabba, C., Collettini, C., Piccinini, D., & Cocco, M. (2007). Architecture and mechanics of an active low-angle normal fault: Alto Tiberina fault, Northern Apennines, Italy. *Journal of Geophysical Research: Solid Earth*, *112*(B10). doi: 10.1029/2007JB005015

Chicco, J., Verdoya, M., Giuli, G., & Invernizzi, C. (2019). Thermophysical properties and mineralogical composition of the Umbria-Marche carbonate succession (central Italy). *Geological Society of America Special Paper*(542), 59–67. doi: 10.1130/2019.2542(02)

Chiodini, G., Cardellini, C., Amato, A., Boschi, E., Caliro, S., Frondini, F., & Ventura, G. (2004). Carbon dioxide Earth degassing and seismogenesis in central and southern Italy. *Geophysical Research Letters*, *31*(7), L07615. doi: 10.1029/2004GL019480

Ciccotti, M., Almagro, R., & Mulargia, F. (2004). Static and dynamic moduli of the seismogenic layer in Italy. *Rock mechanics and rock engineering*, *37*, 229–238. doi: 10.1007/s00603-003-0019-7

Clements, T., & Denolle, M. A. (2018). Tracking groundwater levels using the ambient seismic field. *Geophysical Research Letters*, *45*(13), 6459–6465. doi: 10.1029/2018GL077706

Collettini, C., Tesei, T., Scuderi, M. M., Carpenter, B. M., & Viti, C. (2019). Beyond Byerlee friction, weak faults and implications for slip behavior. *Earth and Planetary Science Letters*, *519*, 245–263. doi: 10.1016/j.epsl.2019.05.011

D'Agostino, N., Silverii, F., Amoroso, O., Convertito, V., Fiorillo, F., Ventafridda, G., & Zollo, A. (2018). Crustal deformation and seismicity modulated by groundwater recharge of karst aquifers. *Geophysical Research Letters*, *45*(22), 12–253. doi: 10.1029/2018GL079794

Dahm, T., & Fischer, T. (2014). Velocity ratio variations in the source region of earthquake swarms in NW Bohemia obtained from arrival time double-differences. *Geophysical Journal International*, *196*(2), 957–970. doi: 10.1093/gji/ggt410

Dill, R. (2008). Hydrological model LSDM for operational Earth rotation and gravity field variations. *Scientific Technical Report 08/09*. doi: 11.2312/GFZ.b103-08095

Dill, R., & Dobslaw, H. (2013). Numerical simulations of global-scale high-resolution hydrological crustal deformations. *Journal of Geophysical Research: Solid Earth*, *118*(9), 5008–5017. doi: 0.1002/jgrb.50353

Dong, D., Fang, P., Bock, Y., Cheng, M., & Miyazaki, S. (2002). Anatomy of apparent seasonal variations from GPS-derived site position time series. *Journal of Geophysical Research: Solid Earth*, *107*(B4), ETG–9. doi: 10.1029/2001JB000573

Dorman, J., & Ewing, M. (1962). Numerical inversion of seismic surface wave dispersion data and crust-mantle structure in the New York-Pennsylvania area. *Journal of Geophysical Research*, *67*(13), 5227–5241. doi: 10.1029/JZ067i013p05227

ECMWF. (n.d.). *European Centre for Medium Range Weather Forecasts.* Retrieved from `https://https://www.ecmwf.int/` (Last accessed: March 12, 2024)

EPOS. (n.d.). *Near Fault Observatory (NFO).* Retrieved from `https://www.epos-eu.org/tcs/near-fault-observatories/data-services` (Last accessed: March 12, 2024)

Fokker, E., Ruigrok, E., Hawkins, R., & Trampert, J. (2021). Physics-based relationship for pore pressure and vertical stress monitoring using seismic velocity variations. *Remote Sensing*, *13*(14), 2684. doi: 10.3390/rs13142684

Fokker, E., Ruigrok, E., Hawkins, R., & Trampert, J. (2023). 4D physics-based pore pressure monitoring using passive image interferometry. *Geophysical Research Letters*, *50*(5), e2022GL101254. doi: 10.1029/2022GL101254

Freund, D. (1992). Ultrasonic compressional and shear velocities in dry clastic rocks as a function of porosity, clay content, and confining pressure. *Geophysical Journal International*, *108*(1), 125–135. doi: 10.1111/j.1365-246X.1992.tb00843.x

Grêt, A., Snieder, R., & Scales, J. (2006). Time-lapse monitoring of rock properties with coda wave interferometry. *Journal of Geophysical Research: Solid Earth*, *111*(B3). doi: 10.1029/2004JB003354

Gualandi, A., Nichele, C., Serpelloni, E., Chiaraluce, L., Anderlini, L., Latorre, D., . . . Avouac, J.-P. (2017). Aseismic deformation associated with an earthquake swarm in the Northern Apennines (Italy). *Geophysical Research Letters*, *44*(15), 7706–7714. doi: 10.1002/2017GL073687

Gualandi, A., Serpelloni, E., & Belardinelli, M. E. (2016). Blind source separation problem in GPS time series. *Journal of Geodesy*, *90*, 323–341. doi: 10.1007/s00190-015-0875-4

Haney, M. M., & Tsai, V. C. (2017). Perturbational and nonperturbational inversion of Rayleigh-wave velocities. *Geophysics*, *82*(3), F15–F28. doi: 10.1190/GEO2016-0397.1

Herrmann, R. B. (2013). Computer programs in seismology: An evolving tool for instruction and research. *Seismological Research Letters*, *84*(6), 1081–1088. doi: 10.1785/0220110096

Hettema, M. (2020). Analysis of mechanics of fault reactivation in depleting reservoirs. *International Journal of Rock Mechanics and Mining Sciences*, *129*, 104290. doi: 10.1016/j.ijrmms.2020.104290

Hillers, G., Campillo, M., Ben-Zion, Y., & Roux, P. (2014b). Seismic fault zone trapped noise. *Journal of Geophysical Research: Solid Earth*, *119*(7), 5786–5799. doi: 10.1002/2014JB011217

Hillers, G., Campillo, M., & Ma, K.-F. (2014). Seismic velocity variations at TCDP are controlled by MJO driven precipitation pattern and high fluid discharge properties. *Earth and Planetary Science Letters*, *391*, 121–127. doi: 10.1016/j.epsl.2014.01.040

Hillis, R. (2000). Pore pressure/stress coupling and its implications for seismicity. *Exploration Geophysics*, *31*(2), 448–454. doi: 10.1071/EG00448

Hobiger, M., Wegler, U., Shiomi, K., & Nakahara, H. (2012). Coseismic and postseismic elastic wave velocity variations caused by the 2008 Iwate-Miyagi Nairiku earthquake, Japan. *Journal of Geophysical Research: Solid Earth*, *117*(B9). doi: 10.1029/2012JB009402

Hreinsdóttir, S., & Bennett, R. A. (2009). Active aseismic creep on the Alto Tiberina low-angle normal fault, Italy. *Geology*, *37*(8), 683–686. doi: 10.1130/G30194A.1

Illien, L., Andermann, C., Sens-Schönfelder, C., Cook, K., Baidya, K., Adhikari, L., & Hovius, N. (2021). Subsurface moisture regulates himalayan groundwater storage and discharge. *AGU Advances*, *2*(2), e2021AV000398. doi: 10.1029/2021AV000398

Illien, L., Sens-Schönfelder, C., Andermann, C., Marc, O., Cook, K. L., Adhikari, L. B., & Hovius, N. (2022). Seismic velocity recovery in the subsurface: transient damage and groundwater drainage following the 2015 Gorkha earthquake, Nepal. *Journal of Geophysical Research: Solid Earth*, *127*(2), e2021JB023402. doi: 10.1029/2021JB023402

INGV Seismological Data Centre. (2006). *Rete Sismica Nazionale.* Italy: Istituto Nazionale di Geofisica e Vulcanologia (INGV). Retrieved from `http://iside.rm.ingv.it/instruments` (Last accessed: March 12, 2024) doi: 10.13127/SD/X0FXNH7QFY

Ji, S., Li, L., Motra, H. B., Wuttke, F., Sun, S., Michibayashi, K., & Salisbury, M. H. (2018). Poisson's ratio and auxetic properties of natural rocks. *Journal of Geophysical Research: Solid Earth*, *123*(2), 1161–1185. doi: 10.1002/2017JB014606

Khaksar, A., Griffiths, & McCann. (2001). Compressional-and shear-wave velocities as a function of confining stress in dry sandstones. *Geophysical Prospecting*, *47*(4), 487–508. doi: 10.1046/j.1365-2478.1999.00146.x

Kimman, W., & Trampert, J. (2010). Approximations in seismic interferometry and their effects on surface waves. *Geophysical Journal International*, *182*(1), 461–476. doi: 10.1111/j.1365-246X.2010.04632.x

Latorre, D., Mirabella, F., Chiaraluce, L., Trippetta, F., & Lomax, A. (2016). As-sessment of earthquake locations in 3-D deterministic velocity models: A case study from the Altotiberina Near Fault Observatory (Italy). *Journal of Geophysical Research: Solid Earth*, *121*(11), 8113–8135. doi: 10.1002/2016JB013170

Liu, C., Aslam, K., & Daub, E. (2020). Seismic velocity changes caused by water table fluctuation in the New Madrid seismic zone and Mississippi embayment. *Journal of Geophysical Research: Solid Earth*, *125*(8), e2020JB019524. doi: 10.1029/2020JB019524

Louie, J. N. (2001). Faster, better: shear-wave velocity to 100 meters depth from refraction microtremor arrays. *Bulletin of the Seismological Society of America*, *91*(2), 347–364. doi: 10.1785/0120000098

Maeda, T., Sato, H., & Nishimura, T. (2008). Synthesis of coda wave envelopes in randomly inhomogeneous elastic media in a half-space: single scattering model including Rayleigh waves. *Geophysical Journal International*, *172*(1), 130–154. doi: 10.1111/j.1365-246X.2007.03603.x

Mandler, E., Pintori, F., Gualandi, A., Anderlini, L., Serpelloni, E., & Belardinelli, M. E. (2021). Post-seismic deformation related to the 2016 Central Italy seismic sequence from GPS displacement time-series. *Journal of Geophysical Research: Solid Earth*, *126*(9), e2021JB022200. doi: 10.1029/2021JB022200

Meier, U., Shapiro, N. M., & Brenguier, F. (2010). Detecting seasonal variations in seismic velocities within Los Angeles basin from correlations of ambient seismic noise. *Geophysical Journal International*, *181*(2), 985–996. doi: 10.1111/j.1365-246X.2010.04550.x

Mikhael, N., Poli, P., & Garambois, S. (2024). Non-linear seismic velocity variations observed during a seismic swarm in the Alto Tiberina low angle normal fault from ambient noise correlation measurements. *Journal of Geophysical Research: Solid Earth*, *129*(2), e2023JB028232. doi: 10.1029/2023JB028232

Miller, S. A., Collettini, C., Chiaraluce, L., Cocco, M., Barchi, M., & Kaus, B. J. (2004). Aftershocks driven by a high-pressure CO_2source at depth. *Nature*, *427*(6976), 724–727. doi: 10.1038/nature02251

Miller, S. A., Nur, A., & Olgaard, D. L. (1996). Earthquakes as a coupled shear stress-high pore pressure dynamical system. *Geophysical Research Letters*, *23*(2), 197–200. doi: 10.1029/95GL03178

Minato, S., Tsuji, T., Ohmi, S., & Matsuoka, T. (2012). Monitoring seismic velocity change caused by the 2011 Tohoku-oki earthquake using ambient noise records. *Geophysical Research Letters*, *39*(9). doi: 10.1029/2012GL051405

Momoi, T. (1981). Scattering of Rayleigh wave at a vertical boundary. *Journal of Physics of the Earth*, *29*(5), 435–485. doi: 10.4294/jpe1952.29.435

Montone, P., & Mariucci, M. T. (2020). Constraints on the structure of the shallow crust in central Italy from geophysical log data. *Scientific reports*, *10*(1), 3834. doi: 10.1038/s41598-020-60855-0

Pan, Y., Chen, R., Ding, H., Xu, X., Zheng, G., Shen, W., … Li, S. (2019). Common mode component and its potential effect on GPS-inferred three-dimensional crustal deformations in the Eastern Tibetan Plateau. *Remote Sensing*, *11*(17), 1975. doi: 10.3390/rs11171975

Pastoressa, A. E., Murru, M., Taroni, M., Console, R., Montuori, C., Falcone, G., & Di Stefano, R. (2023). Temporal Variations of Seismicity Rates and Gutenberg–Richter b-Values for a Stochastic Declustered Catalog: An Example in Central Italy. *Seismological Society of America*(94), 1566–1578. doi: 10.1785/0220220298

Piana Agostinetti, N., Giacomuzzi, G., & Chiarabba, C. (2017). Seismic swarms and diffuse fracturing within Triassic evaporites fed by deep degassing along the low-angle Alto Tiberina normal fault (Central Apennines, Italy). *Journal of Geophysical Research: Solid Earth*, *122*(1), 308–331. doi: 10.1002/2016JB013295

Pintori, F., Serpelloni, E., & Gualandi, A. (2022). Common-mode signals and vertical velocities in the greater Alpine area from GNSS data. *Solid Earth*, *13*(10), 1541–1567. doi: 10.5194/se-13-1541-2022

Pintori, F., Serpelloni, E., Longuevergne, L., Garcia, A., Faenza, L., D'Alberto, L., ... Belardinelli, M. E. (2021). Mechanical response of shallow crust to groundwater storage variations: Inferences from deformation and seismic observations in the Eastern Southern Alps, Italy. *Journal of Geophysical Research: Solid Earth*, *126*(2), e2020JB020586. doi: 10.1029/2020JB020586

Poli, P., Marguin, V., Wang, Q., D'Agostino, N., & Johnson, P. (2020). Seasonal and coseismic velocity variation in the region of L'Aquila from single station measurements and implications for crustal rheology. *Journal of Geophysical Research: Solid Earth*, *125*(7), e2019JB019316. doi: 10.1029/2019JB019316

Poupinet, G., Ellsworth, W., & Frechet, J. (1984). Monitoring velocity variations in the crust using earthquake doublets: An application to the Calaveras Fault, California. *Journal of Geophysical Research: Solid Earth*, *89*(B7), 5719–5731. doi: 10.1029/JB089iB07p05719

Progetto ViDEPI. (2009-2023). *Visibility of Petroleum Exploration Data in Italy.* Ministero dello sviluppo economico DGRME - Società Geologica Italiana - Assomineraria. Retrieved from https://www.videpi.com/videpi/pozzi/regione.asp?ub=T

Pushpalatha, R., Perrin, C., Le Moine, N., Mathevet, T., & Andréassian, V. (2011). A downward structural sensitivity analysis of hydrological models to improve low-flow simulation. *Journal of hydrology*, *411*(1-2), 66–76. doi: 10.1016/j.jhydrol.2011.09.034

Quattrocchi, F. (1999). In search of evidence of deep fluid discharges and pore pressure evolution in the crust to explain the seismicity style of the Umbria-Marche 1997-1998 seismic sequence (Central Italy). *Annali di Geofisica*, *42*(4), 609–636. Retrieved from http://hdl.handle.net/2122/1398 doi: 10.4401/ag-3743

Rice, J. (1992). Fault stress states, pore pressure redistributions, and the Weakness of the San Andreas Fault. In *Fault Mechanics and Transport Properties of Rocks* (eds. Evans, B. & Wong, T.F.). , *51*, 475–503.

Riddell, A. R., King, M. A., & Watson, C. S. (2020). Present-day vertical land motion of Australia from GPS observations and geophysical models. *Journal of Geophysical Research: Solid Earth*, *125*(2), e2019JB018034. doi: 10.1029/2019JB018034

Rivet, D., Brenguier, F., & Cappa, F. (2015). Improved detection of preeruptive seismic velocity drops at the piton de la fournaise volcano. *Geophysical Research Letters*, *42*(15), 6332–6339. doi: 10.1002/2015GL064835

Rovida, A., Locati, M., Camassi, R., Lolli, B., & Gasperini, P. (2020). The Italian earthquake catalogue CPTI15. *Bulletin of Earthquake Engineering*, *18*(7), 2953–2984. doi: 10.1007/s10518-020-00818-y

Sens-Schönfelder, C., & Wegler, U. (2006). Passive image interferometry and seasonal variations of seismic velocities at Merapi volcano, Indonesia. *Geophysical research letters*, *33*(21). doi: 10.1029/2006GL027797

Serpelloni, E., Cavaliere, A., Martelli, L., Pintori, F., Anderlini, L., Borghi, A., ... others (2022). Surface velocities and strain-rates in the Euro-Mediterranean region from massive GPS data processing. *Frontiers in Earth Science*. doi: 10.3389/feart.2022.907897

Serpelloni, E., Faccenna, C., Spada, G., Dong, D., & Williams, S. D. (2013). Vertical GPS ground motion rates in the Euro-Mediterranean region: New evidence of velocity gradients at different spatial scales along the Nubia-Eurasia plate boundary. *Journal of Geophysical Research: Solid Earth*, *118*(11), 6003–6024. doi: 10.1002/2013JB010102

Serpelloni, E., & Pintori, F. (2024). *Displacement time series from GNSS stations in the Alto Tiberina Fault area (Central Italy) [Data set].* Zenodo. Retrieved from https://zenodo.org/records/10809324 doi: 10.5281/zenodo.10809324

Serpelloni, E., Pintori, F., Gualandi, A., Scoccimarro, E., Cavaliere, A., Anderlini, L., ... Todesco, M. (2018). Hydrologically Induced Karst Deformation: Insights From GPS Measurements in the Adria-Eurasia Plate Boundary Zone. *Journal of Geophysical Research: Solid Earth*, *123*(5), 4413–4430. doi: 10.1002/2017JB015252

Servizio Idrografico Regione Umbria. (2021–2024). *Servizio Idrografico Regione Umbria.* Retrieved from https://annali.regione.umbria.it/ (Last accessed: March 12, 2024)

Shapiro, S. A. (2003). Elastic piezosensitivity of porous and fractured rocks. *Geophysics*, *68*(2), 482–486. doi: 10.1190/1.1567215

Silverii, F., d'Agostino, N., Métois, M., Fiorillo, F., & Ventafridda, G. (2016). Transient deformation of karst aquifers due to seasonal and multiyear groundwater variations observed by GPS in Southern Apennines (Italy). *Journal of Geophysical Research: Solid Earth*, *121*(11), 8315–8337. doi: 10.1002/2016JB013361

Snieder, R. (1986). 3-D linearized scattering of surface waves and a formalism for surface wave holography. *Geophysical Journal International*, *84*(3), 581–605. doi: 10.1111/j.1365-246X.1986.tb04372.x

Snieder, R. (2006). The theory of coda wave interferometry. *Pure and Applied geophysics*, *163*(2-3), 455–473. doi: 10.1007/s00024-005-0026-6

Snieder, R., Grêt, A., Douma, H., & Scales, J. (2002). Coda wave interferometry for estimating nonlinear behavior in seismic velocity. *Science*, *295*(5563), 2253–2255. doi: 10.1126/science.1070015

Socco, L., & Strobbia, C. (2004). Surface-wave method for near-surface characterization: A tutorial. *Near surface geophysics*, *2*(4), 165–185. doi: 10.3997/1873-0604.2004015

Soldati, G., Zaccarelli, L., & Faenza, L. (2019). Spatio-temporal seismic velocity variations associated to the 2016–2017 central Italy seismic sequence from noise cross-correlation. *Geophysical Journal International*, *219*(3), 2165–2173. doi: 10.1093/gji/ggz429

Szelwis, R., & Behle, A. (1984). Shear-wave velocity of the weathering zone from multimodal Rayleigh waves. In *Seg technical program expanded abstracts 1984* (pp. 721–723). Society of Exploration Geophysicists. doi: 10.1190/1.1894225

Tarantola, A., & Valette, B. (1982). Generalized nonlinear inverse problems solved using the least squares criterion. *Reviews of Geophysics*, *20*(2), 219–232. doi: 10.1029/RG020i002p00219

Trippetta, F., Collettini, C., Vinciguerra, S., & Meredith, P. (2010). Laboratory measurements of the physical properties of Triassic Evaporites from Central Italy and correlation with geophysical data. *Tectonophysics*, *492*(1-4), 121–132. doi: 10.1016/j.tecto.2010.06.001

Tsai, V. C. (2011). A model for seasonal changes in GPS positions and seismic wave speeds due to thermoelastic and hydrologic variations. *Journal of Geophysical Research: Solid Earth*, *116*(B4). doi: 10.1029/2010JB008156

Tuan, H.-S. (1975). On bulk waves excited at a groove by Rayleigh waves. *Journal of Applied Physics*, *46*(1), 36–41. doi: 10.1063/1.321345

Vadacca, L., Casarotti, E., Chiaraluce, L., & Cocco, M. (2016). On the mechanical behaviour of a low-angle normal fault: the Alto Tiberina fault (Northern Apennines, Italy) system case study. *Solid Earth*, *7*(6), 1537–1549. doi: 10.5194/se-7-1537-2016

Valoroso, L., Chiaraluce, L., Di Stefano, R., & Monachesi, G. (2017). Mixed-mode slip behavior of the Altotiberina low-angle normal fault system (Northern Apennines, Italy) through high-resolution earthquake locations and repeating events. *Journal of Geophysical Research: Solid Earth*, *122*(12), 10–220. doi: 10.1002/2017JB014607

Van den Bogert, P., & van Eijs, R. (2020). Why Mohr-circle analyses may underestimate the risk of fault reactivation in depleting reservoirs. *International Journal of Rock Mechanics and Mining Sciences*, *136*, 104502. doi: 10.1016/j.ijrmms.2020.104502

Voisin, C., Guzmán, M. A. R., Refloch, A., Taruselli, M., & Garambois, S. (2017). Groundwater monitoring with passive seismic interferometry. *Journal of Water Resource and Protection*, *9*(12), 1414–1427. doi: 10.4236/jwarp.2017.912091

Volpe, G., Pozzi, G., Carminati, E., Barchi, M. R., Scuderi, M. M., Tinti, E., ... Collettini, C. (2022). Frictional controls on the seismogenic zone: Insights from the Apenninic basement, Central Italy. *Earth and Planetary Science Letters*, *583*, 117444. doi: 10.1016/j.epsl.2022.117444

Vuan, A., Brondi, P., Sugan, M., Chiaraluce, L., Di Stefano, R., & Michele, M. (2020). Intermittent slip along the Alto Tiberina Low-Angle Normal Fault in Central Italy. *Geophysical Research Letters*, *47*(17), e2020GL089039. doi: 10.1029/2020GL089039

Wathelet, M., Jongmans, D., & Ohrnberger, M. (2004). Surface-wave inversion using a direct search algorithm and its application to ambient vibration measurements. *Near surface geophysics*, *2*(4), 211–221. doi: 10.3997/1873-0604.2004018

White, A. M., Gardner, W. P., Borsa, A. A., Argus, D. F., & Martens, H. R. (2022). A review of GNSS/GPS in hydrogeodesy: Hydrologic loading applications and their implications for water resource research. *Water Resources Research*, *58*(7), e2022WR032078. doi: 10.1029/2022WR032078

Xia, J., Miller, R. D., & Park, C. B. (1999). Estimation of near-surface shear-wave velocity by inversion of Rayleigh waves. *Geophysics*, *64*(3), 691–700. doi: 10.1190/1.1444578

Yates, A., Savage, M., Jolly, A., Caudron, C., & Hamling, I. (2019). Volcanic, co-seismic, and seasonal changes detected at White Island (Whakaari) volcano, New Zealand, using seismic ambient noise. *Geophysical Research Letters*, *46*(1), 99–108. doi: 10.1029/2018GL080580

Zaccarelli, L., Shapiro, N., Faenza, L., Soldati, G., & Michelini, A. (2011). Variations of crustal elastic properties during the 2009 L'Aquila earthquake inferred from cross-correlations of ambient seismic noise. *Geophysical research letters*, *38*(24). doi: 10.1029/2011GL049750

Zoback, M. D., & Zinke, J. C. (2002). Production-induced normal faulting in the Valhall and Ekofisk oil fields. *Pure and applied geophysics*, *159*(1), 403–420. doi: 10.1007/PL00001258